Epithelial colonies *in vitro* elongate through collective effects

Jordi Comelles[1], Soumya SS[2], S. Anvitha[3], Guillaume Salbreux[4], Frank Jülicher[5,6], Mandar M. Inamdar[2#], Daniel Riveline[1]*

[1]Laboratory of Cell Physics ISIS/IGBMC, CNRS and University of Strasbourg, Strasbourg, France; Institut de Génétique et de Biologie Moléculaire et Cellulaire, Illkirch, France; Centre National de la Recherche Scientifique, UMR7104, Illkirch, France; Institut National de la Santé et de la Recherche Médicale, U964, Illkirch, France; Université de Strasbourg, Illkirch, France.
[2]Department of Civil Engineering, Indian Institute of Technology Bombay, Powai, Mumbai 400076, INDIA.
[3]Department of Mechanical Engineering, Indian Institute of Technology Bombay, Powai, Mumbai 400076, INDIA.
[4]The Francis Crick Institute, 1 Midland Road, London NW1 1AT, United Kingdom.
[5]Max Planck Institute for the Physics of Complex Systems, Nöthnitzer Str. 38, 01187 Dresden, Germany.
[6]Cluster of Excellence Physics of Life, TU Dresden, Germany.

Electronic address: #minamdar@iitb.ac.in, *riveline@unistra.fr

Abstract

Epithelial tissues of the developing embryos experience symmetry breaking through elongation and shape transformations by different mechanisms, such as neighbour exchange, cell elongation, and oriented cell division. Although the molecular actors involved in these phenomena are known, the mesoscopic processes leading to the different mechanisms remain elusive. This knowledge gap exists, in part, because autonomous tissue self-organization in vivo *is influenced by interactions with external inputs, such as morphogen gradients or neighbouring tissues, and it is difficult to distinguish intrinsic from directed tissue behaviour. Here we use* in vitro *experiments to observe the spontaneous elongation behaviour of spreading circular epithelial colonies prepared with microfabrication. By using cell biology methods and by quantifying colony deformation kinematics at multiple scales, we report that the global elongation direction of the colony correlates with the direction of local protrusions at the colony boundary and also with the anisotropy in the average cell elongation within colony. Although we see no mean bias in the direction of elongation for a freely spreading colony, the axis of this global symmetry breaking can be imposed by an external time-periodic stretch. Moreover, tissue elongation happens primarily due to cell elongations and orientated neighbour exchange, respectively, in the absence and in the presence of external force. These different behaviours are confirmed by theory using a vertex model for collective cell behaviour. This provides a framework to understand autonomous tissue elongation and its cellular origins.*

Introduction

Tissue elongation is a central morphogenetic event occurring in many organisms during development (Lecuit and Lenne, 2007; Guillot and Lecuit, 2013), such as *Drosophila* or

C. elegans. The tissue is transformed both in terms of area and shape. Such transformation takes place within typically hour timescale with or without cell division. During this process, symmetry of cells and tissues is broken by different mechanisms, such as neighbor exchange (Rauzi *et al.*, 2008; Rauzi, Lenne and Lecuit, 2010), cell elongation (Clarletta, Ben Amar and Labouesse, 2009; Vuong-Brender, Yang and Labouesse, 2016) and oriented cell division (Campinho *et al.*, 2013). Rearrangement of neighboring cells or T1 transitions is essential in the germ band extension of *Drosophila* (Rauzi *et al.*, 2008; Rauzi, Lenne and Lecuit, 2010), allowing a group of cells to change their position by intercalation, eventually leading to tissue elongation. Cell deformation drives the 3-fold elongation process in *C. elegans* (Clarletta, Ben Amar and Labouesse, 2009; Vuong-Brender, Yang and Labouesse, 2016) while keeping the number of cells and their positions fixed. Finally, epithelial spreading during zebrafish epiboly is promoted by oriented cell divisions as a mechanism to limit tension (Campinho *et al.*, 2013). Those mechanisms can act alone or in combination as in *Drosophila* pupal wing elongation (Etournay *et al.*, 2015). While the phenomenon is known to involve remodeling of adherens junctions (Rauzi, Lenne and Lecuit, 2010) and acto-myosin (He *et al.*, 2010; Rauzi, Lenne and Lecuit, 2010) at the molecular level, mesoscopic mechanisms leading to distinct morphogenesis processes are poorly understood. This is partly because inputs from morphogen gradients (Gilmour, Rembold and Leptin, 2017) or from neighboring tissues (Zhang *et al.*, 2011; Etournay *et al.*, 2015) can affect tissue autonomous self-organization *in vivo*. For example, changes in tissue shape can be influenced by neighboring tissues such as the cuticle and the blade in the *Drosophila* pupal wing elongation (Etournay *et al.*, 2015), the coordination between amnioserosa and epidermis in dorsal closure (Hayes and Solon, 2017), and the muscle layer in gut development (Shyer *et al.*, 2013) or in *C. elegans* morphogenesis (Zhang *et al.*, 2011). Since *in vivo*, epithelial tissues are surrounded by other tissues and the cellular dynamics leading to elongation can result from interactions between tissues and boundary conditions, it is therefore difficult to disentangle cell intrinsic from externally mediated behaviors. In this context, it appears important to characterize elongation in an *in vitro* system where the epithelial tissue undergoes shape transition autonomously.

Here we use *in vitro* experiments and numerical simulations to characterize the spontaneous behavior of a growing cell colony *in vitro*. We designed an assay to study the spontaneous elongation of a tissue that is not subjected to external orienting input, we studied the appearance of the symmetry breaking, and the effect that external forces have in this process. We show that *in vitro* tissue elongation arises from anisotropy in the average cell elongation. This anisotropy sets the direction along which boundary cells migrate radially outwards resulting in a non-isotropic elongation that arises primarily through cell elongation. For colonies submitted to a time periodic stretch, the axis of global symmetry breaking can be imposed by external force, and tissue elongation arises through oriented neighbor exchange. Emergence of radially migrating cells and the interplay between cell elongation and cell rearrangements are confirmed by numerical simulations based on a vertex model. Our results suggest that spontaneous shape deformation is related to the mean orientation of the nematic cell elongation field in the absence of any external input. This provides a framework to explain autonomous tissue elongation and how contributions from different mesoscopic mechanisms can be modulated by external forces.

Results

Isotropic colonies elongate in a non-isotropic manner. To study the spontaneous tissue deformation arising during epithelial growth, we designed an *in vitro* assay to track symmetry breaking, both spontaneous and driven by external force. We prepared isotropic colonies of Madin Darby Canine Kidney (MDCK) cells, which assume features of epithelial cells *in vivo* (Reinsch and Karsenti, 1994; Adams *et al.*, 1998; Reffay *et al.*, 2014), such as adherens junctions (Adams *et al.*, 1998), cytoskeletal components and the Rho signaling pathway regulating cell shapes and dynamics (Reffay *et al.*, 2014; Fodor *et al.*, 2018). The initial size and shape of the colonies were controlled by plating cells in microfabricated circular stencils (Ostuni *et al.*, 2000) of 250 µm in diameter (Figure 1a), the typical coherence length of such epithelial tissues (Doxzen *et al.*, 2013). When cells reached confluency, the stencil was removed at t_0. Strikingly, circular colonies were initially surrounded by an acto-myosin cable (Figure 1 – figure supplement 1). Cell dynamics was followed over time by phase contrast (Movie 1) or fluorescence microcopy with strains labeled with GFP cadherin (Figure 1b), that allowed to observe the behavior of individual cells. We observed that colonies expanded in a non-isotropic manner (Figure 1c).

In order to compare elongations in each experiment, we quantified the breaking of symmetry by ellipse-fitting the colony. Shape change analysis was quantified by a nematic shape elongation tensor $\boldsymbol{Q}$. It has two independent components defined as $Q_{xx} = ½ \ln(a/b)\cos(2\bullet\theta)$ and $Q_{xy} = ½ \ln(a/b)\sin(2\bullet\theta)$, where a corresponds to the major axis, b to the minor axis, and θ to the orientation of the major axis of the ellipse (Figure 1d). As can be seen in Figure 1e, MDCK colonies elongated persistently along the main axis of elongation ($Q_{xx} > 0$ and $Q_{xy} \approx 0$) for 6 hours. We note that elongation observed during this time was similar in magnitude to tissue elongation observed during *in vivo* morphogenesis, for instance in the wing blade in *Drosophila* (Etournay *et al.*, 2015). Moreover, the elongation direction ($\theta_{\text{final}} = \theta(t = 6\text{ h})$) converges to a constant value within 2 hours after t_0 (Figure 1f). As a result, we focus here on these first 2 hours during which the elongation axis is established.

Cyclic stretching rectifies symmetry breaking. It has been previously described for *C. elegans* embryo elongation (Zhang *et al.*, 2011) and in other organisms (Zhang and Labouesse, 2012) that time periodic stretch can play a role in morphogenesis. Motivated by these observations, we explored whether oscillatory external forces could have an impact on the direction of elongation. We designed an experimental set-up where elongating colonies were submitted to cyclic stretching (Figure 2a and Movie 2). Mechanical cycles of contraction-relaxation can range from 1 s in *C. elegans* epithelial elongation (Zhang *et al.*, 2011) up to 200 s in dorsal closure (Solon *et al.*, 2009). So, we explored frequencies and extensions around physiological values (Zhang and Labouesse, 2012). We selected three different cycle durations (20 s, 60 s, and 120 s period) and three different stretching conditions (5%, 10% and 15% strain). The stretch was applied to a silicon membrane and was transmitted to the colony. Figure 2 – figure supplement 1 shows the value of the components of the tensor $\boldsymbol{Q}$ along time for the different strains and periods tested. Among conditions, we observed colony elongation along the direction imposed by the external strain when we stretched cyclically with 60 s timescale and 5% strain (Figure 2b and Movie 3). The overall elongation of colonies under cyclic stretching was similar to the spontaneous elongation in the absence of external forces during the first two hours (Figure 2c). Also, the components of the nematic shape elongation tensor $\boldsymbol{Q}$ under cyclic stretching were comparable to the spontaneous elongation of colony when stretch was not applied but oriented in the direction of external force (Figure 2d).

Therefore, an external cyclic force can rectify symmetry breaking and set the direction of tissue elongation.

Collective effects are essential for rectification. To get further insight into the collective nature of the rectification of tissue elongation, we probed the roles of adhesion between cells. First, we stretched single MDCK cells, individually plated. We observed that cells oriented perpendicularly to the external force (Figures 3a and 3b) as previously reported for fibroblasts (Faust *et al.*, 2011).Then we blocked cell-cell junction in circular colonies prior stretching. Briefly, we incubated confluent colonies in medium containing 5 mM EDTA and 10 µg/ml anti- E-cadherin blocking antibody that targeted the extracellular domain of E-cadherin for 30 min (Harris, Daeden and Charras, 2014). Then, medium was replaced by normal medium and the evolution of colonies with and without stretch was followed (Figure 3c). In the absence of external force, colonies elongated in a non-isotropic manner (Figure 3d). Under cyclic stretching, elongation was also non-isotropic and along the direction perpendicular to the external force, in contrast to the parallel elongation observed when cell-cell contacts were intact (Figure 2b-d). This supports the collective nature of colony elongation. It is worth noting that cells inside the colony exhibited a decrease in their mean velocity (Figure 3e) and a large recruitment of myosin within cells similar to reinforcements (Riveline *et al.*, 2001) in stretching conditions, as shown by the appearance of stress fibers (Figure 3f). However, this effect did not appear to affect the overall elongation rate. Altogether these data suggest that the asymmetric expansion of colonies in the direction imposed by an external force is generally associated to a collective effect.

Fingers and symmetry breaking. We next sought to identify the source of symmetry breaking in both conditions, with and without an external force. It has previously been reported that in MDCK monolayers, cells can migrate tangentially to the monolayer boundary when confined (Doxzen *et al.*, 2013), or perpendicular to the boundary in the form of multicellular groups or fingers during monolayer expansion (Reffay *et al.*, 2011, 2014). During spontaneous elongation of MDCK colonies in the absence of external forces (Movie 4), we observed that boundary cells tend to move either perpendicularly or tangentially to the colony boundary (Figure 4a). In most of the experiments, an acto-myosin cable, similar to compartmentalization boundaries *in vivo* (Monier *et al.*, 2010; Calzolari, Terriente and Pujades, 2014), was observed in the outer boundary of the colonies at stencil removal (Figure 1 – figure supplement 1). When this supra-cellular structure was intact, cells at the periphery are reported to undergo clockwise and counter clockwise rotations (Doxzen *et al.*, 2013). In contrast, when a local interruption of this cable appeared, the cell at the vicinity extended lamellipodia and moved away and radially from the center of the colony (Figure 4 – figure supplement 1a). Apparently, a local defect in the cable could promote the local protrusion of a cell in the direction normal to the edge as shown in laser ablation experiments previously (Reffay *et al.*, 2014). Several local defects could appear within the same colony, thus providing the opportunity for cells in the vicinity to protrude outwards. This cell has been termed leader cell (Reffay *et al.*, 2011) and the collection of cells protruding from the circular colonies along this cell can be identified as the finger-like structures already reported for MDCK monolayers (Reffay *et al.*, 2011, 2014).
We performed cell tracking and observed that, on average, these protruding cells are faster than other boundary cells (Figure 4a and Figure 4 – figure supplement 1b and 1c). They are characterized also by radial and directional migrations, in contrast to tangential motion observed in the other cells of the outer region of the colony (Figure 4 – figure

supplement 1d and 1e). In general, the motion of these so-called leader cells was directionally persistent and on average the shape of the whole colony followed the same overall direction (Figure 4b and 4c). To correlate colony elongation with leader cell orientation, we analyzed the evolution of a larger number of colonies for 2 hours after stencil removal (Movie 4). We quantified the breaking of symmetry by fitting an ellipse to the shape of each colony. We then tracked the positions where finger-like structures were appearing, as well as the direction and distance performed by each of them. We could observe that the elongation direction of the whole colony correlated on average with the direction of the leader cell migration and associated finger (Figure 4c).
We then measured the position and displacement for each finger in control colonies and colonies under cyclic stretching (Figure 4d). We observed that, when growing parallel to the direction of force application, finger cells performed larger displacements than when growing perpendicularly, whereas no bias was observed in the absence of external force. To further explore this effect, we grew MDCK monolayers with straight boundaries either parallel or perpendicular to the external force. Then, we let fingers appear and grow for 2 hours before applying cyclic stretching (Figure 4e). When fingers were growing perpendicular to the stretching direction, they shrank upon application of cyclic stretching; in contrast, fingers further elongated when parallel to the direction of external forces. Altogether, this suggests that direction of finger-like structures correlates with elongation direction, and that external stretching affects the dynamics of finger growth.

Collective effects and symmetry breaking. Finger growth correlates with colony elongation. However, if it is a cause or consequence of the symmetry breaking of the shape of the colony, remains elusive. We observed that when a finger moves outward from the colony, cells in the immediate vicinity elongate and seem to reorient their elongation axis towards the finger (Figure 5a). Recent studies have shown that the nematic field of cell elongation and its topological defects could be involved in the growth of bacterial colonies (Doostmohammadi, Thampi and Yeomans, 2016) and in controlling dynamics, death and extrusion of epithelial cells (Kawaguchi, Kageyama and Sano, 2017; Saw *et al.*, 2017; Mueller, Yeomans and Doostmohammadi, 2019). We wondered if the spontaneous elongation of colonies would also be related to the average cell elongation. We followed the evolution of the cell elongation nematic field in different colonies during expansion. We first obtained the spatio-temporal cell elongation nematic orientation field $\phi(x, y, t)$ (see Methods) on the experimental time-lapse images (see Figure 5b, Figure 5 – figure supplement 1a-c, Movie 5 and Supplementary Material Section IC). We could then obtain the angle θ_{nematic} of the average cell-shape nematic field at t_0 which we compared with final colony orientation θ_{colony} obtained using the ellipse fitting analysis (Figure 5c, Figure 5 – figure supplement 1d and Supplementary Material Section IC). Strikingly, we observed a clear average cell elongation even at the time of stencil removal t_0, and the corresponding angle θ_{nematic} correlated with colony orientation when elongation direction was established (Figure 5d, Figure 5 – figure supplement 1d and 1e). The cell elongation orientation field $\phi(x, y, t)$ was not homogeneous at t_0 but exhibited a complex pattern with ±½ topological defects (Figure 5b and Supplementary Material Section ID). Interestingly, an expression that provides equilibrium orientation of liquid crystals with defects and having one constant Frank free energy,

$$\phi(x, y)_{\text{fit}} = \alpha + \sum_i k_i \frac{y - y_i}{x - x_i}, \qquad (1)$$

mimics the experimentally observed orientation field $\phi(x, y)$ very well with just one fitting parameter α (see Supplementary Material Section ID for details.) Here $k_i = \pm½$ and (x_i, y_i) are the strength and location, respectively, of the topological defects obtained from

the experimental image. Since the orientation of tissue elongation correlates with orientation of average cell elongation at t_0, this suggests that leader cells moving outward from the colony are not the cause of symmetry breaking in colony shape, but rather follow from the initial cell shape elongation before stencil removal.

Contributions to symmetry breaking. We next sought to evaluate quantitatively the contribution of cellular processes to elongation. We quantified the contributions of each cellular event using image segmentation, cell tracking and neighbor triangulation (Etournay *et al.*, 2015, 2016) (see Supplementary Material Section IA, Figure 6a and 6b, Figure 6 – figure supplement 1 and Figure 6 – figure supplement 2, and Movie 6). This procedure decomposes overall tissue elongation, which is quantified in terms of cumulative total pure shear, into contributions from cell elongation and topological changes. Five main events contribute to total shear: cell elongation change, cell division, cell extrusion, T1 transition, and correlation effects (Etournay *et al.*, 2015, 2016). At the colony scale, shear decomposition plots (Figure 6c and Figure 6 – figure supplement 3) revealed that the total pure shear gives values consistent with elongation estimates from ellipse fitting (Figure 6d). Note that various contributions to shear decomposition exhibit significant variability between experiments (Figure 6 – figure supplement 3). However, we found that after the first 2 hours, the contribution of cell elongation is generally comparable to the total pure shear, with a smaller contribution from other sources (Figure 6d). When looking at the shear decompositions of colonies under cyclic stretching (Figure 6e and Figure 6 – figure supplement 3), the cumulative shear values were also similar to the ones obtained by ellipse fitting (Figure 6f). Interestingly, we found however that in that case, shear created by T1 transitions is the main contributor for the total pure shear, while cell elongation does not contribute to tissue elongation (Figure 6f and Figure 6 – figure supplement 3). This indicates that applying oscillatory forces to the tissue changes fundamentally the main mode of tissue elongation by favoring topological rearrangements of the cell network.

Vertex model recapitulates symmetry breaking and shear decomposition. We then asked whether a model could reproduce experimental observations of shear decomposition and, in particular, in which conditions tissue elongation would arise from cell elongation or from topological transitions. We developed a vertex model which takes into account mechanical anisotropies such as active stresses and polarized cell bond tension (see Figure 7a and Supplementary Material Section II). We generated a confluent colony of circularly confined cells, in which a unit director **p** that represented the cell polarity was assigned to each cell. Based on orientation of the director, each cell generated an extensile active stress $\boldsymbol{\sigma}_a$ and bias λ in the base value of its edge contractility to promote cell elongation and active T1 transitions. We assumed that the experimentally measured cell elongation nematic **q** is a readout of the underlying cell polarity **p** (Figure 7b). Hence, the initial spatial distribution of **p** was based on the commonly observed pattern of **q** (Figure 7c). To evolve **p** with time, we imposed that **p** of the exterior cells tended to be parallel to the boundary, whereas the inner cells tended to align their **p** with those of their neighbors (Supplementary Material Section IID).

Upon removal of confinement, we found that the simulated colony spontaneously elongates, in a direction set by the orientation of the mean cell elongation nematic field, along with the formation of finger-like structures near the +½ defect, as observed experimentally (see Movie 7). Our simulations therefore reproduce experimental observations indicating that colony deformation can be understood without forces exerted by a leader cell at the colony boundary (Figure 7c, Movie 7, and Supplementary Material

Section II). To test whether we could also recapitulate different contributions of the total pure shear inside the tissue, we performed a shear decomposition analysis of *in silico* Movies. We found a qualitatively similar cumulative shear-strain decomposition as was observed in experiments (Figure 7d and 7e), where the main contribution came from cell elongation. Moreover, by changing the relative contributions of the cellular active stress magnitude (σ_a) and the edge tension bias (λ), we could modulate the relative contributions from cell elongations and T1 transitions to the total pure shear (Figure 7 – figure supplement 1) as was also observed in experiments with colonies in the absence or presence of cyclic stretching (Figure 6 – figure supplement 3). When σ_a was dominant, the colony elongation was primarily due to cell elongation, whereas when λ was the stronger term, T1 transitions were the main cause of colony elongation. These results reveal possible cellular mechanisms that can govern the process of tissue deformation and influence whether cell elongation, or cellular rearrangements, dominate tissue elongation.

Discussion

Tissue spreading is key during embryonic development (Bénazéraf *et al.*, 2010; Campinho *et al.*, 2013; Etournay *et al.*, 2015). Epithelial cells migrate in a collective and cohesive manner. In many cases symmetry is broken leading to shape transformation. The resulting tissue kinematics and the underlying mechanisms for this symmetry breaking has been studied using original approaches, and is understood with a variety of cell-based and continuum models *in vivo* (Blanchard *et al.*, 2009; Clarletta, Ben Amar and Labouesse, 2009; Aigouy *et al.*, 2010; Etournay *et al.*, 2015; Guirao *et al.*, 2015; Alt, Ganguly and Salbreux, 2017). On the *in vitro* situation too, combination of theory and experiments have been applied on similar phenomena (Mark *et al.*, 2010; Tarle *et al.*, 2015; Kawaguchi, Kageyama and Sano, 2017; Saw *et al.*, 2017).

In the present work, we sought to integrate knowledge from *in vitro* and *in vivo* studies to test new ideas for breaking symmetry through collective effects. First we showed that initially circular epithelial colonies spontaneously expanded in a non-isotropic manner and the elongation observed was similar in magnitude to *Drosophila* wing blade elongation *in vivo* (Etournay *et al.*, 2015). However, the undeformed circular colonies have a non-zero average cell elongation even before spreading starts, which determines orientation of the final colony shape. Our analysis also showed that the cell orientation patterns are not homogeneous but spatially organized and directed by the presence of ±½ topological defects. It was already shown that topological defects in the cell elongation nematic field have a key role on epithelial dynamics (Kawaguchi, Kageyama and Sano, 2017) and on cell death and extrusion (Saw *et al.*, 2017). Our results reinforce the idea that cell elongation nematic field, which could only arise from collective interaction between cells, can have an impact on epithelial morphogenesis.

Since developing tissues are regularly subjected to internal oscillations (Solon *et al.*, 2009; He *et al.*, 2010; Rauzi, Lenne and Lecuit, 2010) and external pulsatory forces (Zhang *et al.*, 2011; Hayes and Solon, 2017) in a number of living organisms, we explored the effect of external forces in the *in vitro* circular colonies. We observed that the direction of elongation could be rectified by imposing an external cyclic force. This particular behavior is of great interest from an *in* vivo point of view: cyclic contraction could direct elongation in specific directions to trigger the next steps in morphogenesis. The generic localizations of muscles connected to epithelial layer (Zhang and Labouesse, 2012) could have this essential function for tissues which would otherwise elongate in any direction

like in our assay. Finally, direction of this tissue rectification is along the external force, but perpendicular to the reorientation of single cell under external stretching, and this further supports the collective nature of the phenomenon.

We also systematically quantified the shear deformation kinematics of the colony and demonstrated that some of the colonies exhibit shear decomposition patterns similar to those observed during *Drosophila* pupal wing elongation (Etournay *et al.*, 2015). Moreover, while the colony deformation for the control colonies was dominated by cell elongation, T1 transitions were the main drivers of the colony shape anisotropy under cyclic stretching thus indicating different mechanisms at work. Thus, the current work thus makes a direct comparison and contrast tissue kinematics between *in vivo* and *in vitro* cases.

Finally, we developed a vertex model that takes into account mechanical anisotropies. Cell anisotropic active stress arising in the cell core, cortical contractility at the cell-cell junctions and cell motility are three of the important forces involved in morphogenesis of epithelial monolayers. To our knowledge, this is the first attempt to systematically show how each of these activities acts on tissue kinematics. Specifically, we showed that cell anisotropic active stress results mainly in cell elongation whereas anisotropies in cortical contractility primarily effects cell intercalations or T1 transitions. Including cell motilities appears to enhance tissue shear generated by the other two modes of internal forcing.

From our simulations, we could demonstrate that symmetry breaking and finger formation in colonies and the corresponding tissue kinematics observed in our experiments could be brought about by collective active behavior of the colony cells and does not require special action of leader cells (Theveneau and Linker, 2017). This result echoes experiments in which the emergence of the leader cells and the fingering behavior at the border were suggested to arise due to the internal stress pattern in the tissue (Vishwakarma *et al.*, 2018). On the other hand, there are many excellent models in which the boundary cells are ascribed special motility properties that could replicate the experimental results on border fingering (Mark *et al.*, 2010; Tarle *et al.*, 2015). Thus, although leader cells at the boundary may play a role in the border fingering, our experimental findings and simulations clearly indicate that the cell-level internal activities and cell-cell interactions are sufficient to cause symmetry breaking in the colony shape and its overall kinematics via the collective cell-shape nematic field.

Conclusion

Our results show that cell elongation nematic field can have an impact on epithelia morphogenesis. It was already reported that topological defects in the cell elongation nematic field have a key role on epithelial dynamics (Kawaguchi, Kageyama and Sano, 2017) and on cell death and extrusion (Saw *et al.*, 2017). Now, we showed that circular epithelial colonies when in confinement build up a mean nematic orientation. This symmetry breaking results from the inner activity of cells, and sets the direction for colony elongation. Epithelia changes in shape could be revisited *in vivo* with this new framework, leading to potential generic rule of morphogenesis in developmental biology.

Materials and Methods

Cell culture. MDCK cells (GFP-E-cadherin strain (Adams *et al.*, 1998), GFP-Actin strain, RFP-LifeAct / GFP-myosin strain (Klingner *et al.*, 2014)) were cultured in Dulbecco's modified Eagle medium (D-MEM) 1g/l glucose (Invitrogen), supplemented with 10% fetal bovine serum (FBS) (Invitrogen) and 1% penicillin-streptomycin (and the corresponding resistance for each strain). Cells were passaged every 2-3 days using standard procedures.

Fabrication of PDMS membranes and stencils. Poly(dimethylsiloxane) (PDMS) (Sylgard) was prepared by mixing the pre-polymer and the cross-linker at a 10:1 ratio. To prepare stretchable membranes, uncured PDMS was first centrifuged (3000 rpm for 5 min) to remove air bubbles. Afterwards, the PDMS was spin-coated on a flat polystyrene (PS) surface (500 rpm for 1 min) and cured at 65ºC overnight. PDMS stencils were prepared as described previously (Ostuni *et al.*, 2000). Briefly, SU-8 2050 molds containing circles of 250 µm in diameter were prepared by standard photolithography. Uncured PDMS was then spin-coated on molds to a thickness lower than the height of the microstructures (50 µm) and cured overnight at 65ºC. Stencils for the finger experiments were prepared by spin-coating uncured PDMS on a flat surface.

Cell seeding on stencils. The PDMS stencils were cut, peeled off the mold, and placed in a 2% Pluronic F-127 (Sigma-Aldrich) in PBS for 1 h. The stencils were then kept in PBS for 2h and dried under the hood flow. PDMS stretchable membranes were cut and then activated using O_2 plasma. The membranes and the stencils were exposed to UV light in the cell culture hood for 10 min. Afterwards, stretchable membranes were incubated with fibronectin 20 µg/ml for 1 h, rinsed with PBS and dried. PDMS membranes were placed on a PS holder, and the PDMS stencils were deposited on top of the membrane right after. A rectangular PDMS chamber was attached onto the membrane using vacuum grease, and cells were seeded at a density of 20000 cells/mm^2 (Serra-Picamal *et al.*, 2012) for 4 h. When cells were attached, the medium was changed and the membrane with the cells was kept in the incubator. Local cell density could vary within each colony. We followed the dynamics of assembly of the colony prior removal of the stencil and we could see that cellular clusters size distribution and respective location within the cavity at plating could contribute to these variations. Once they formed confluent circular colonies, the stencils were removed with tweezers carefully before starting the experiment. Some of the colonies exhibited elongation in the short time window between stencil removal and the start of image acquisition.

Time-lapse microscopy. After stencil removal, the medium was replaced by L-15 (Leibovitz's L-15 medium, Invitrogen) supplemented with 10% FBS. Cells were then observed under a Nikon Ti inverted microscope using either a x10 or a x20 objective for 6 h at 37ºC. Images were acquired every 5 min.

Stretching experiments. The stretching device was designed in the lab. Briefly, a Thorlabs motor (Thorlabs z812 motor, Thorlabs) was controlling the motion of a PDMS membrane, and everything was mounted on a custom-made microscope stage. Circular colonies were plated on PDMS membranes, and after removal of the stencils, samples were placed on the microscope. Cyclic stretches were applied and images were taken every 30 minutes typically shortly to prevent interfering with the time course of the experiments. We probed 3 times for cycles, 20s, 60s, 120s, and 3 extensions, 5%, 10%, and 20%. The shape of the cycles was triangular. We checked that the PDMS stencils were elastic at all extension and frequency ranges.

Chemical treatments. To prevent the formation of E-cadherin-mediated adhesion, cells were incubated for 30min with L-15 medium containing 5 mM EDTA (Sigma-Aldrich) and 10 µg/ml anti-E-cadherin blocking antibody that targeted the extracellular domain of E-cadherin (Gumbiner, Stevenson and Grimaldi, 1988) (uvomorulin, monoclonal anti-E-cadherin antibody, Sigma); after incubation, the medium was replaced by normal L-15 and the experiment started.

Finger dynamics experiments. For the finger test after growth, we let finger grow for 2 hours, and we subsequently applied the cyclic stretch.

Colony shape change analysis. Shape change analysis was performed using ImageJ (http://rsb.info.nih.gov/ij, NIH). The outline of the colony on phase contrast images was ellipse fitted at every time point. Major axis a, minor axis b, and ellipse orientation θ were obtained. We computed $\boldsymbol{Q}$, defined as $Q_{xx}(t) = ½ \ln(a(t)/b(t))\cdot\cos 2\cdot(\theta(t) - \theta(t_{final}))$ and $Q_{xy}(t) = ½\ln(a(t)/b(t))\cdot\sin 2\cdot(\theta(t) - \theta(t_{final}))$ to quantify cell colony elongation. In stretching experiments, the x axis corresponds to the direction of the external stretch and $\boldsymbol{Q}$ components are defined as $Q_{xx}(t) = ½ \ln(a(t)/b(t))\cdot\cos 2\cdot(\theta(t))$ and $Q_{xy}(t) = ½\ln(a(t)/b(t))\cdot\sin 2\cdot(\theta(t))$.

Velocity analysis. The centroid trajectories of cells were tracked using the manual tracking plug-in in ImageJ. Data analysis was performed using a custom-made code in MATLAB (The MathWorks). Cell positions were characterized by a vector $\mathbf{r}(t)$, with t denoting time and $\mathbf{r}$ position in space (bold letter refers to a vector). Every recorded cell position during the time-lapse experiment was defined as $\mathbf{r}_i = \mathbf{r}(t_i)$, where $t_i = i\Delta t$ are the times of recording and Δt denotes the duration of time-lapses. The average velocity of each cell was then defined as $v = (1/T)\cdot\sum_i r_i$, being r_i the module of the vector $\mathbf{r}_i$ and T the total duration of the trajectory.

Colony segmentation and cell tracking. Movies acquired using a MDCK GFP-E-cadherin strain were first pre-processed with FIJI. The *subtract background* function was applied to remove noise. Images were then loaded to Tissue Analyzer (TA) v8.5 (Aigouy *et al.*, 2010) for edge detection and cell tracking.

Orientation field of the cells and topological defects. First, the background noise of the time-lapse images of the elongating colonies was reduced with the *subtract background* function by using a rolling ball radius of 40 px. The resulting images were then subjected to *band-pass* filter with upper and lower limits of 40 px and 3 px, respectively. The background noise from this output was reduced by using the *subtract background* command again with a rolling ball radius of 40 px. The processed images from each experiment were analyzed with the OrientationJ plugin of FIJI to quantify their local spatial orientation that reflects the underlying cell elongation. Within this plugin we used a local smoothing window of 20 px (approximately of the size of the cells) to obtain the *structure tensor* at discrete points on a grid of 20 px × 20 px. The plugin provides the dominant direction ϕ_i of the structure tensor at each point (x_i, y_i) that represents the local *orientation* field $q_i = \cos\phi_i\, e_1 + \sin\phi_i\, e_2$ for cell elongation. The OrientationJ plugin also provides the *coherence* C of the structure tensor to quantify the strength of the orientation; $C \approx 0$ and $C \approx 1$ would approximately correspond to rounded and elongated cells, respectively. The orientation or the director field $\mathbf{q}$ thus obtained was further quantified by studying the spatiotemporal evolution of ±1/2 topological defects

that were obtained by calculating the winding number over unit-cells of the underlying grid. The local smoothing window of 20 px for obtaining the *structure tensor*, which is approximately of the size of cells, ensured that the most robust defects were observed. The validity of this procedure was cross-verified with the smoothed cell-shape nematic field and the corresponding ±½ defects from the segmented and triangulated data of the experiments processed in Tissue Miner (TM) (Figure 5 – figure supplement 1 and Supplementary Material Section I). Finally, the orientation of mean cell-shape nematic calculated at 0 hr was compared with shape orientation of the colony at t = 2 hrs. See Supplementary Material Section I for more details (also see Movie 5).

Quantification of cellular deformations, topological transitions and their contribution to pure shear deformation. After obtaining the geometrical and topological information of the colonies from the series tracked images generated using TA, TM was used to extract, triangulate and store the data with the help of an automated workflow. The database obtained after this stage of analysis was used to quantify various state properties such as cell area, neighbor number, cell elongation and the contribution of different cellular processes to deformation using scripts written both in *R* and in *Python*. TM was further used to quantify the contributions of various cellular events such as cell elongation and topological transitions to the colony deformation. More details about this analysis can be found in Supplementary Material Section I (also see Movie 6).

Vertex Model Simulations. A vertex model was developed with an addition of a unit nematic director **p** to every cell. The orientation of the boundary cell **p** was maintained parallel to the boundary, whereas **p** for internal cells were modeled to tend to align with the **p** of its neighbors. In these simulations, an extensile active stress $\sigma_a(\mathbf{pp}-\frac{1}{2}\mathbf{1})$ acts to increase cell elongation along **p**. In addition, a bias λ was also applied on the basic edge tension with respect to the director **p** of its neighboring cells. This bias reduces (increases) the tension of the edge along (perpendicular to) **p**. Consequently, the closure (formation) of edges is enhanced in the direction perpendicular (parallel) to **p**. Hence, the T1 transitions in the region around the cells are oriented to cause shear elongation (contraction) along (perpendicular) to **p**. The colony is provided with an initial condition for **p** that mimics the initial configuration of many experimentally observed cell shape nematic field **q** with two +½ defects that are separated by a distance. The initial polar vector orientation along the nematic axis are chosen at random such that the total polarity is zero, and the dynamics of polarity reorientation is independent on a **p** → **-p** flipping of the polarity axis. To begin with, the cell positions and director orientations were evolved under colony confinement until cell position and **p** do not change significantly. The confinement is then removed to see how the colony breaks symmetry in its shape. In another set of simulations, a small motility v_0 was also provided to the internal cells (Figure 7 – figure supplement 1). Similar to the experiments, the output of these simulations was also processed in TM and analyzed for topological defects and pure shear decomposition. More details of the simulations are provided in Supplementary Material Section II (also see Movie 7).

Statistics. No statistical methods were used to predetermine sample size. Measurements were performed on different colonies (n) obtained in different independent experiments (N). The exact values are defined at the caption of each figure. Data presentation (as Mean value ± standard deviation (SD) or as Mean value ± standard error of the mean (SE)) is defined at the corresponding figure caption. D'Agostino normality test, Mann-Whitney

test and Pearson's correlation were performed using GraphPad Prism 8. Specific values are noted at the corresponding figure captions.

Acknowledgments

We acknowledge M. Popovic and R. Etournay for stimulating discussions and help with Tissue Miner, J. Nelson, P. Silberzan, S. Coscoy for sharing the MDCK strains, and J. Prost, K. Dayal and M. Zapotocky for helpful suggestions, David Rodriguez and the Riveline Lab. D.R. and M.M.I. thank MPI-PKS and MPI-CBG for hospitality and many interactions. D.R. acknowledges support from CNRS (ATIP), ciFRC Strasbourg, the University of Strasbourg, Labex IGBMC, Foundation Cino del Duca. This study with the reference ANR-10-LABX-0030-INRT has been also supported by a French state fund through the Agence Nationale de la Recherche under the frame programme Investissements d'Avenir labelled ANR-10-IDEX-0002-02. M.M.I. acknowledges funding from Department of Biotechnology, Government of India (BT/06/IYBA/2012) and Industrial Research and Consultancy Center (IRCC), IIT Bombay. G.S. was supported by the Francis Crick Institute which receives its core funding from Cancer Research UK (FC001317), the UK Medical Research Council (FC001317), and the Wellcome Trust (FC001317).

Competing interests

The authors declare no competing interests.

References

Adams, C. L. *et al.* (1998) 'Mechanisms of Epithelial Cell–Cell Adhesion and Cell Compaction Revealed by High-resolution Tracking of E-Cadherin– Green Fluorescent Protein', *The Journal of Cell Biology*, 142(4), pp. 1105–1119. doi: 10.1083/jcb.142.4.1105.

Aigouy, B. *et al.* (2010) 'Cell Flow Reorients the Axis of Planar Polarity in the Wing Epithelium of Drosophila', *Cell*, 142(5), pp. 773–786. doi: 10.1016/j.cell.2010.07.042.

Alt, S., Ganguly, P. and Salbreux, G. (2017) 'Vertex models: From cell mechanics to tissue morphogenesis', *Philosophical Transactions of the Royal Society B: Biological Sciences*, 372(1720). doi: 10.1098/rstb.2015.0520.

Bénazéraf, B. *et al.* (2010) 'A random cell motility gradient downstream of FGF controls elongation of an amniote embryo.', *Nature*, 466(7303), pp. 248–252. doi: 10.1038/nature09151.

Blanchard, G. B. *et al.* (2009) 'Tissue tectonics: morphogenetic strain rates, cell shape change and intercalation', *Nature Methods*, 6(6), pp. 458–464. doi: 10.1038/nmeth.1327.

Calzolari, S., Terriente, J. and Pujades, C. (2014) 'Cell segregation in the vertebrate hindbrain relies on actomyosin cables located at the interhombomeric boundaries', *EMBO Journal*, 33(7), pp. 686–701. doi: 10.1002/embj.201386003.

Campinho, P. *et al.* (2013) 'Tension-oriented cell divisions limit anisotropic tissue tension in epithelial spreading during zebrafish epiboly.', *Nature Cell Biology*, 15(12), pp. 1405–14. doi: 10.1038/ncb2869.

Clarletta, P., Ben Amar, M. and Labouesse, M. (2009) 'Continuum model of epithelial morphogenesis during caenorhabditis elegans embryonic elongation', *Philosophical Transactions of the Royal Society A: Mathematical, Physical and Engineering Sciences*, 367(1902), pp. 3379–3400. doi: 10.1098/rsta.2009.0088.

Doostmohammadi, A., Thampi, S. P. and Yeomans, J. M. (2016) 'Defect-Mediated Morphologies in Growing Cell Colonies', *Physical Review Letters*, 117(4), pp. 1–5. doi: 10.1103/PhysRevLett.117.048102.

Doxzen, K. *et al.* (2013) 'Guidance of collective cell migration by substrate geometry', *Integrative Biology*, 5, pp. 1026–1035. doi: 10.1039/C3IB40054A.

Etournay, R. *et al.* (2015) 'Interplay of cell dynamics and epithelial tension during morphogenesis of the Drosophila pupal wing', *eLife*, 4(JUNE2015), pp. 1–51. doi: 10.7554/eLife.07090.

Etournay, R. *et al.* (2016) 'TissueMiner: A multiscale analysis toolkit to quantify how cellular processes create tissue dynamics', *eLife*, 5(MAY2016), pp. 1–28. doi: 10.7554/eLife.14334.

Faust, U. *et al.* (2011) 'Cyclic stress at mHz frequencies aligns fibroblasts in direction of zero strain.', *PloS ONE*, 6(12), p. e28963. doi: 10.1371/journal.pone.0028963.

Fodor, É. *et al.* (2018) 'Spatial Fluctuations at Vertices of Epithelial Layers: Quantification of Regulation by Rho Pathway', *Biophysical Journal*, 114(4), pp. 939–946. doi: 10.1016/j.bpj.2017.12.026.

Gilmour, D., Rembold, M. and Leptin, M. (2017) 'From morphogen to morphogenesis and back', *Nature*, 541(7637), pp. 311–320. doi: 10.1038/nature21348.

Guillot, C. and Lecuit, T. (2013) 'Mechanics of Epithelial Tissue Homeostasis and Morphogenesis', *Science*, 340(6137), pp. 1185–1189. doi: 10.1126/science.1235249.

Guirao, B. *et al.* (2015) 'Unified quantitative characterization of epithelial tissue development', *eLife*, 4(DECEMBER2015), pp. 1–52. doi: 10.7554/eLife.08519.

Gumbiner, B., Stevenson, B. and Grimaldi, a. (1988) 'The role of the cell adhesion molecule uvomorulin in the formation and maintenance of the epithelial junctional complex.', *The Journal of Cell Biology*, 107(4), pp. 1575–1587. doi: 10.1083/jcb.107.4.1575.

Harris, A. R., Daeden, A. and Charras, G. T. (2014) 'Formation of adherens junctions leads to the emergence of a tissue-level tension in epithelial monolayers.', *Journal of Cell Science*, pp. 2507–2517. doi: 10.1242/jcs.142349.

Hayes, P. and Solon, J. (2017) 'Drosophila dorsal closure: An orchestra of forces to zip shut the embryo', *Mechanisms of Development*. 144, pp. 2–10. doi: 10.1016/j.mod.2016.12.005.

He, L. *et al.* (2010) 'Tissue elongation requires oscillating contractions of a basal actomyosin network.', *Nature Cell Biology*, 12(12), pp. 1133–42. doi: 10.1038/ncb2124.

Kawaguchi, K., Kageyama, R. and Sano, M. (2017) 'Topological defects control collective dynamics in neural progenitor cell cultures', *Nature*, 545(7654), pp. 327–331. doi: 10.1038/nature22321.

Klingner, C. *et al.* (2014) 'Isotropic actomyosin dynamics promote organization of the apical cell cortex in epithelial cells.', *The Journal of Cell Biology*, 207(1), pp. 107–21. doi: 10.1083/jcb.201402037.

Lecuit, T. and Lenne, P.-F. P.-F. (2007) ‘Cell surface mechanics and the control of cell shape, tissue patterns and morphogenesis’, *Nat Rev Mol Cell Biol*., 8(8), pp. 633–644. Available at: http://dx.doi.org/10.1038/nrm2222.

Mark, S. *et al.* (2010) ‘Physical model of the dynamic instability in an expanding cell culture’, *Biophysical Journal*, 98(3), pp. 361–370. doi: 10.1016/j.bpj.2009.10.022.

Monier, B. *et al.* (2010) ‘An actomyosin-based barrier inhibits cell mixing at compartmental boundaries in Drosophila embryos.’, *Nature Cell Biology*, 12(1), pp. 60–65; sup pp 1-9. doi: 10.1038/ncb2005.

Mueller, R., Yeomans, J. M. and Doostmohammadi, A. (2019) ‘Emergence of Active Nematic Behavior in Monolayers of Isotropic Cells’, *Physical Review Letters*, 122(4), p. 48004. doi: 10.1103/PhysRevLett.122.048004.

Ostuni, E. *et al.* (2000) ‘Patterning Mammalian Cells Using Elastomeric Membranes’, *Langmuir*, 16(20), pp. 7811–7819.

Rauzi, M. *et al.* (2008) ‘Nature and anisotropy of cortical forces orienting Drosophila tissue morphogenesis.’, *Nature Cell Biology*, 10(12), pp. 1401–10. doi: 10.1038/ncb1798.

Rauzi, M., Lenne, P.-F. and Lecuit, T. (2010) ‘Planar polarized actomyosin contractile flows control epithelial junction remodelling.’, *Nature*, 468(7327), pp. 1110–4. doi: 10.1038/nature09566.

Reffay, M. *et al.* (2011) ‘Orientation and polarity in collectively migrating cell structures: statics and dynamics.’, *Biophysical Journal*, 100(11), pp. 2566–75. doi: 10.1016/j.bpj.2011.04.047.

Reffay, M. *et al.* (2014) ‘Interplay of RhoA and mechanical forces in collective cell migration driven by leader cells.’, *Nature Cell Biology*, 16(3), pp. 217–23. doi: 10.1038/ncb2917.

Reinsch, S. and Karsenti, E. (1994) ‘Orientation of Spindle Axis and Distribution of Plasma Membrane Proteins during Cell Division in Polarized MDCKII Cells’, *The Journal of Cell Biology*, 126(6), pp. 1509–1526.

Riveline, D. *et al.* (2001) ‘Focal contacts as mechanosensors: externally applied local mechanical force induces growth of focal contacts by an mDia1-dependent and rock-independent mechanism’, *The Journal of Cell Biology*, 153(6), pp. 1175–1186. doi: 10.1083/jcb.153.6.1175.

Saw, T. B. *et al.* (2017) ‘Topological defects in epithelia govern cell death and extrusion’, *Nature*, 544(7649), pp. 212–216. doi: 10.1038/nature21718.

Serra-Picamal, X. *et al.* (2012) ‘Mechanical waves during tissue expansion’, *Nature Physics*, 8(8), pp. 628–634. doi: 10.1038/nphys2355.

Shyer, A. E. *et al.* (2013) ‘Villification: How the Gut Gets Its Villi’, *Science*, 342(6155), pp. 212–218. doi: 10.1126/science.1238842.Villification.

Solon, J. *et al.* (2009) ‘Pulsed Forces Timed by a Ratchet-like Mechanism Drive Directed Tissue Movement during Dorsal Closure’, *Cell*, 137(7), pp. 1331–1342. doi: 10.1016/j.cell.2009.03.050.

Tarle, V. *et al.* (2015) ‘Modeling the finger instability in an expanding cell monolayer’, *Integrative Biology*, 7(10), pp. 1218–1227. doi: 10.1039/c5ib00092k.

Theveneau, E. and Linker, C. (2017) ‘Leaders in collective migration: Are front cells

really endowed with a particular set of skills?', *F1000Research*, 6, pp. 1–11. doi: 10.12688/f1000research.11889.1.

Vishwakarma, M. *et al.* (2018) 'Mechanical interactions among followers determine the emergence of leaders in migrating epithelial cell collectives', *Nature Communications*, 9(1). doi: 10.1038/s41467-018-05927-6.

Vuong-Brender, T. T. K., Yang, X. and Labouesse, M. (2016) 'Chapter Thirty-Five - C. elegans Embryonic Morphogenesis', in Wassarman, P. (ed.) *Essays on Developmental Biology, Part A*. Academic Press, pp. 597–616. doi: https://doi.org/10.1016/bs.ctdb.2015.11.012.

Zhang, H. *et al.* (2011) 'A tension-induced mechanotransduction pathway promotes epithelial morphogenesis.', *Nature*, 471(7336), pp. 99–103. doi: 10.1038/nature09765.

Zhang, H. and Labouesse, M. (2012) 'Signalling through mechanical inputs - a coordinated process', *Journal of Cell Science*, 125(13), pp. 3039–3049. doi: 10.1242/jcs.093666.

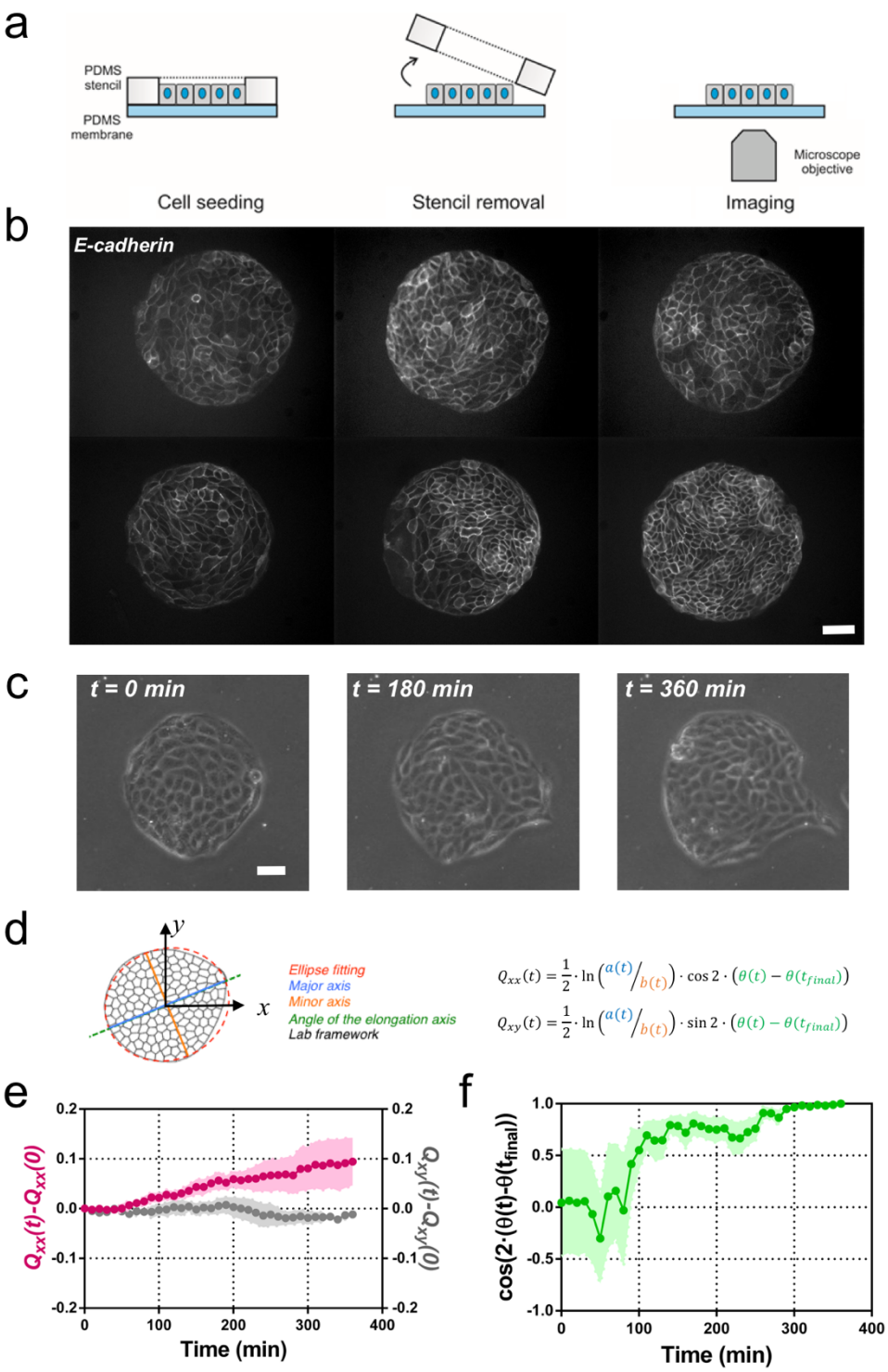

Figure 1. ***Symmetry breaking and its quantification***. (**a**) Schematics of the experimental set-up: MDCK cells were seeded on a PDMS membrane using stencils to predefine their shape. When the colony was confluent, the stencil was removed and the expansion of the colony was observed under the microscope. (**b**) Several examples of MDCK colonies (GFP-E-cadherin) after stencil removal and prior to colony expansion. Scale bar 50 µm. (**c**) Phase contrast images of the spontaneous elongation of a MDCK colony for 360 min. Scale bar 50 µm. (**d**) Colony elongation is quantified by ellipse fitting and Q_{xx} and Q_{xy} measurement referred to the elongation axis. (**e**) Q_{xx} (left y axis) and Q_{xy} (right y axis) during 360 min of colony expansion. Mean value ± standard error of the mean, n = 4 colonies from N = 4 independent experiments. (**f**) Cosine of two times the angle difference between the instantaneous main direction of the colony (θ(t)) and the main

direction of the colony at 360 min ($\theta(t_{final})$). Colonies set the elongation direction within the first 120 min. Mean value ± standard error of the mean, n = 4 colonies from N = 4 independent experiments.

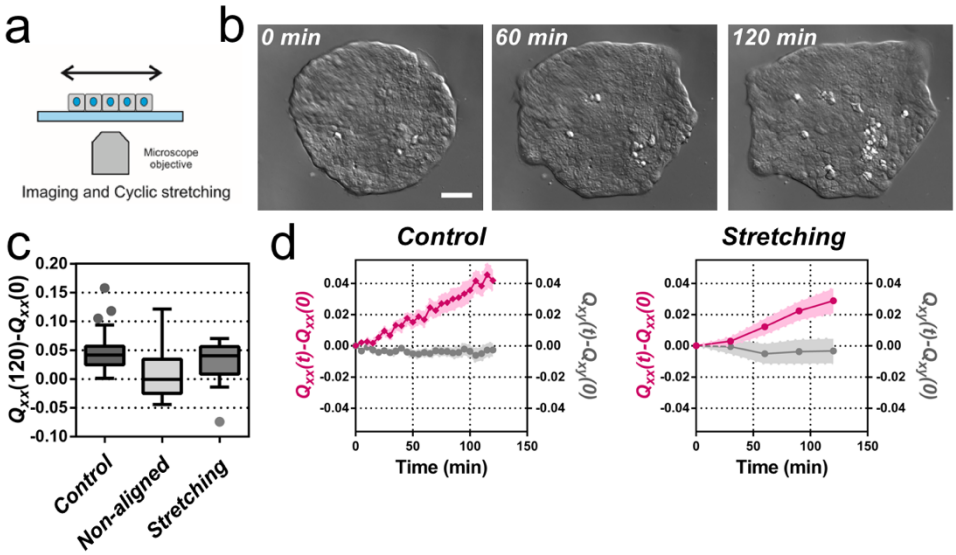

Figure 2. ***Cyclic stretching rectifies symmetry breaking.*** (**a**) Schematics of the experiment where the colony expansion was observed under the microscope while the underlying membrane was stretched. (**b**) Snapshots of the expansion of a MDCK colony while cyclically stretched. Scale bar 50 µm. (**c**) Colony elongation (Q_{xx}) of control colonies along the elongation axis, control colonies in the laboratory framework (non-aligned) and colonies under cyclic stretching in the laboratory framework (stretching). Box Plot between 25th and 75th percentile, being the line in the box the median value, whiskers and outliers (dots) are obtained following Tukey's method, $N_{control} = 11$ independent experiments, n = 25 colonies and $N_{stretching} = 9$, n = 20 colonies. Mann-Whitney test control *vs* control aligned p = 0.0003, control *vs* stretching p = 0.0281 and control aligned *vs* stretching p = 0.3319. (**d**) Q_{xx} (left y axis) and Q_{xy} (right y axis) during 120 min of colony expansion for control colonies and colonies under cyclic stretching. Mean value ± standard error of the mean, $N_{control} = 8$, n = 14 colonies and $N_{stretching} = 9$, n = 20 colonies.

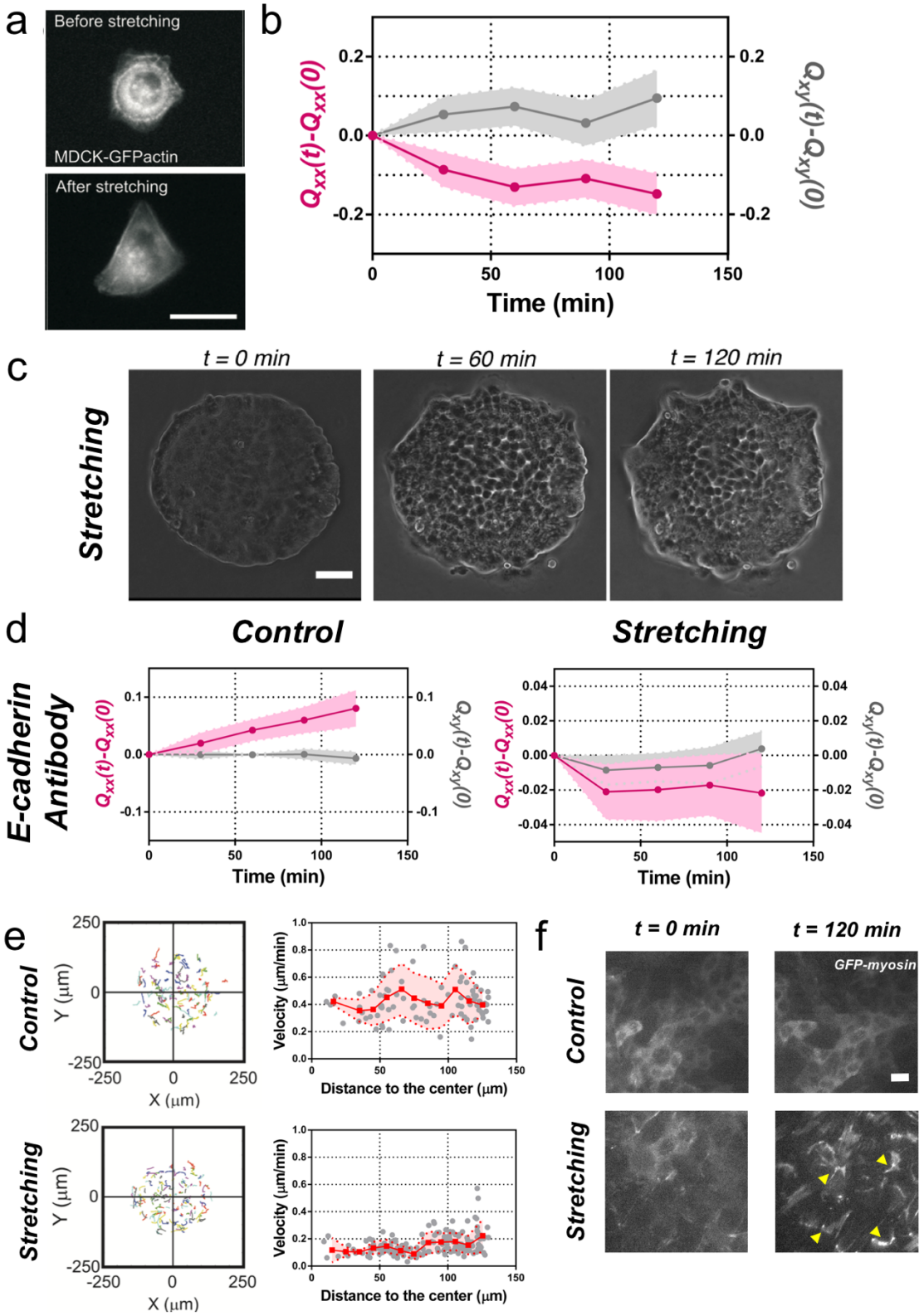

Figure 3. ***Collective effects are essential for rectification***. (**a**) Image of a single MDCK-GFP-actin cell before and after being stretch for 2 hours (5% strain and 60s period). Scale bar 20µm. (**b**) Q_{xx} (left y axis) and Q_{xy} (right y axis) of single cells during 120 min of cyclic stretching. Mean value ± standard error of the mean. N = 3, n = 31 cells. (**c**) Phase contrast images of an MDCK colony evolving for 120 min under cyclic mechanical stretching when E-cadherins are blocked by an E-cadherin antibody. Scale bar 50µm. (**d**) Comparison of the cumulative Q_{xx} (left y axis) and cumulative Q_{xy} (right y axis) during 120 min of colony expansion when E-cadherin are

blocked by an E-cadherin antibody in control and under cyclic stretching. Mean value ± standard error of the mean, $N_{control} = 3$, n = 8 colonies and $N_{stretching} = 4$, n = 15 colonies. (**e**) Trajectories of cells (left) and single cell velocity as a function of its distance to the center of the colony (right) in control colonies (top) and under cyclic stretching (bottom). $n_{control} = 90$ cells from 8 colonies of $N_{control} = 4$ independent experiments and $n_{stretching} = 154$ cells from 13 colonies of $N_{stretching} = 4$ independent experiments. Individual cells in grey, red square and line corresponds mean (binned by distance to the center), shadowed area corresponds to SD. (**f**) Myosin distribution inside MDCK-GFP-myosin colonies at 0 min and at 120 min after expansion in control and under stretching. Note the myosin structures appearing in the stretching case (yellow arrows). Scale bar 10 µm.

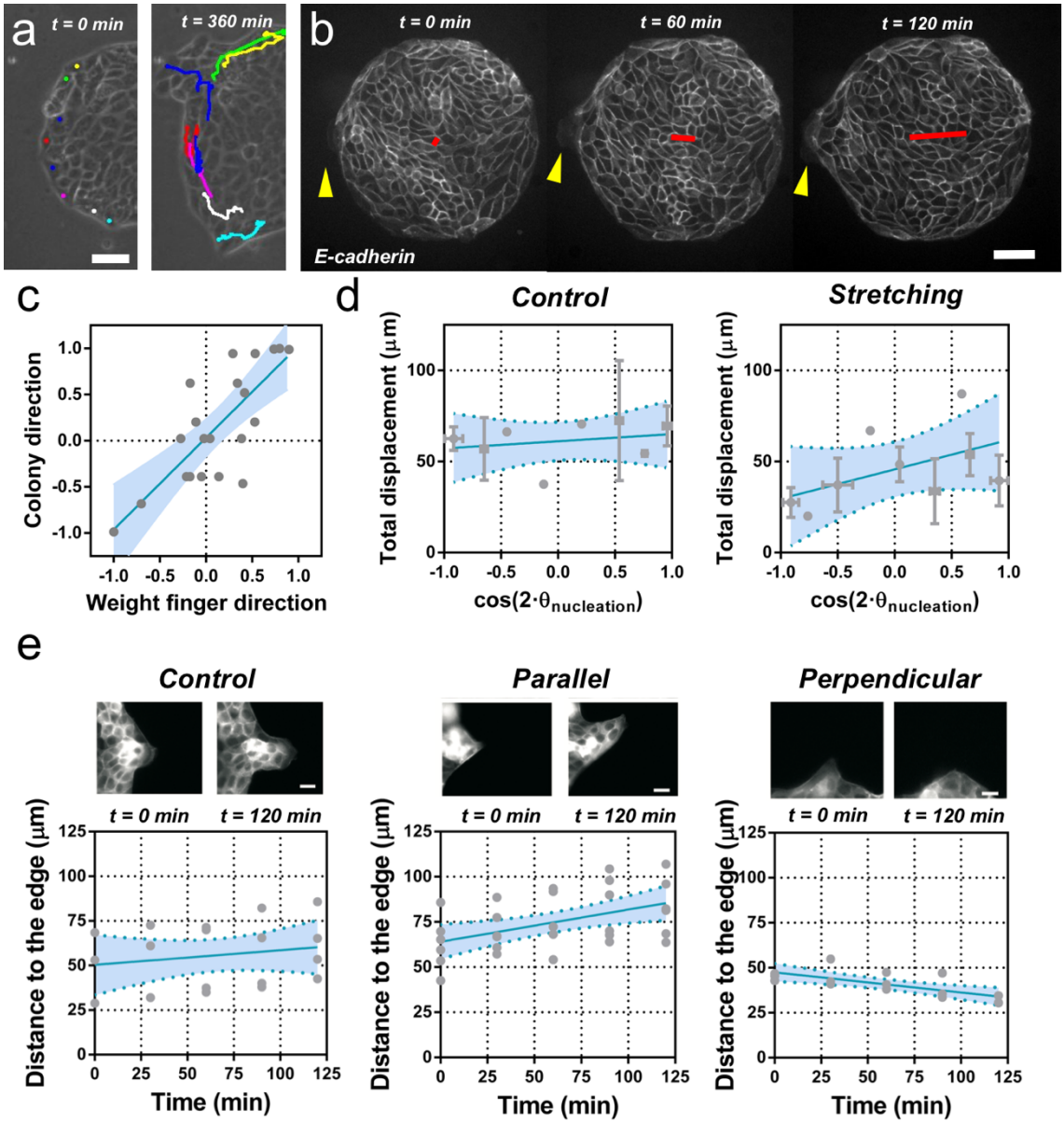

Figure 4. ***Fingers and symmetry breaking***. (**a**) Trajectories of boundary cells during colony expansion. Two types of trajectories are observed: radial and tangential. Scale bar 50 µm. (**b**) Fluorescent images (GFP-E-cadherin) of a colony evolving for 120 min. Red line shows the orientation of the colony according to ellipse fitting (length scales with the change in Q_{xx}) and yellow arrow indicates a cell migrating radially. Scale bar 50 µm. (**c**) Direction of the colony elongation (quantified by the cosine of 2 times the angle of the main axis of the colony at t = 2 hours) as a function of the weight finger direction (quantified by the average of the cosine of 2 times the angle of each finger trajectory, e.g. the angle corresponding to the vector between the position of the finger at t = 0 hours and t = 2 hours, of each finger weight by the finger's displacement). N = 5, $n_{colonies}$ = 12 colonies and n_{finger} = 21 fingers. Blue line corresponds to the linear fitting of the data points and the shadowed area corresponds to the 95% confidence interval. Pearson's correlation coefficient r = 0.7724, p = 0.0001. (**d**) Total displacement of finger growth as a function of its initial position in the colony (angular coordinate from the center of the colony) for control colonies and colonies under stretching. N = 5 independent experiments, $n_{colonies}$ = 11 colonies and n_{finger} = 21 fingers (control) and N = 6, $n_{colonies}$ = 10 colonies and n_{finger} = 28 fingers (stretching). Averaged fingers in grey (both position and distance, Mean ± SD), blue line corresponds to the linear fitting of the data points and the shadowed area corresponds to the 95% confidence interval. (**e**) Distance between the tip of the finger and the edge of the monolayer along time, for monolayers in control conditions, stretched parallel and perpendicular to the finger

growth direction. $N_{control} = 3$, $N_{parallel} = 4$ and $N_{perpendicular} = 3$ independent experiments and n = 4, 6 and 3 fingers respectively. Individual fingers in grey, blue line corresponds to the linear fitting of the data points and the shadowed area corresponds to the 95% confidence interval.

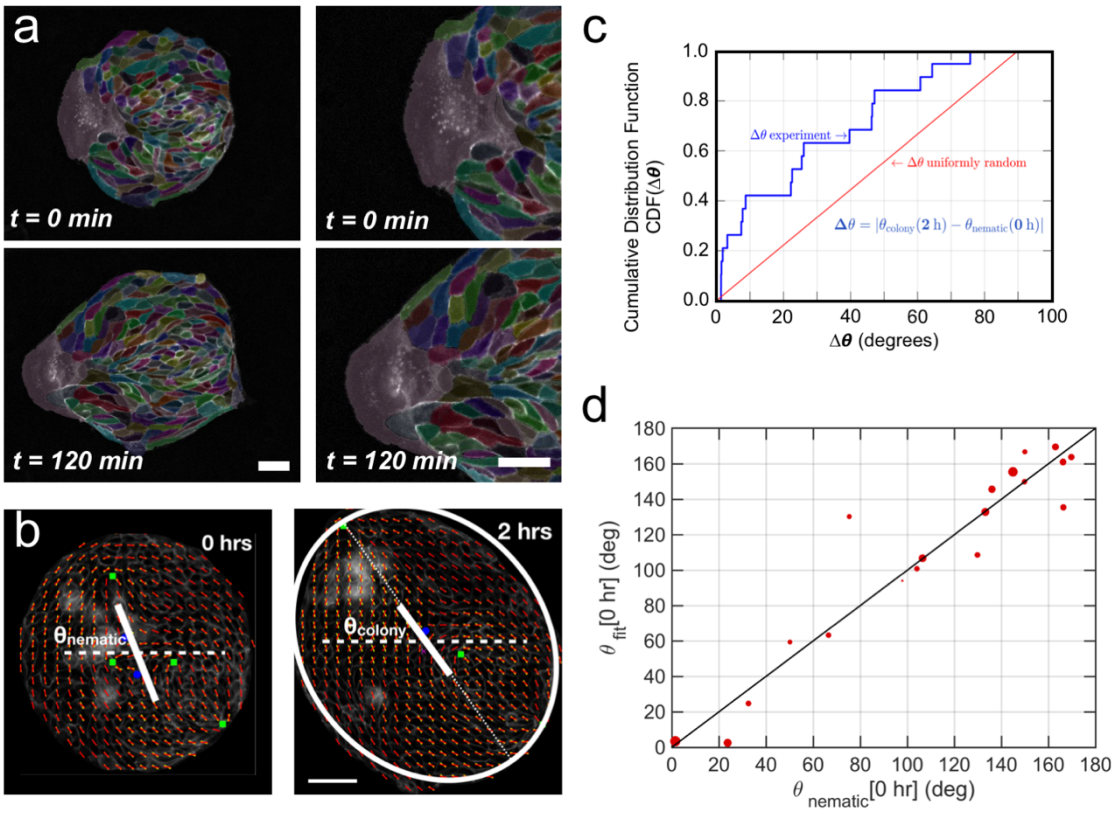

Figure 5. ***Collective effects and symmetry breaking***. (**a**) A leader cell at the boundary of the colony pulls the colony outwards while inner cells deform and elongate. Scale bar 50 µm. (**b**) Cell shape is quantified using a nematic field (red segments). First, the mean cell shape nematic is quantified at the moment of stencil removal (0 hours) and the orientation $\theta_{nematic}$ of its mean for the entire colony is obtained. Then, the overall shape of the colony after 2 hours is obtained by fitting an ellipse, whose major axis makes an angle θ_{colony}. The yellow directors correspond to fits for the cell shape nematic field obtained with respect to the +1/2 and -1/2 topological defects of the experimentally obtained (red) nematic field (also see Supplementary Material Section V for details.) Scale bar 50 µm. (**c**) The cumulative distribution function (CDF) for the difference $\Delta\theta$ between $\theta_{nematic}$ (0 hours) and θ_{colony} (2 hours) is obtained from n = 19 colonies of N = 5 independent experiments. Red line corresponds to the CDF of a random distribution of the difference $\Delta\theta$. This plot shows a strong correlation between the cell shape nematic and the overall shape symmetry breaking (also see Figure 5 – figure supplement 1d, and Supplementary Material Section IE). (**d**) The experimentally measured angle of mean nematic orientation $\theta_{nematic}$ obtained for 19 colonies at t = 0 h is compared with its counterpart θ_{fit} obtained by fitting the experimental data with Eq. 1 of the main paper with respect to the orientation parameter α (see Section ID of Supplementary Material). The size of the red circles in (b) is proportional to the magnitude of anisotropy of the colony shape after 2 h. n = 19 colonies of N = 5 independent experiments.

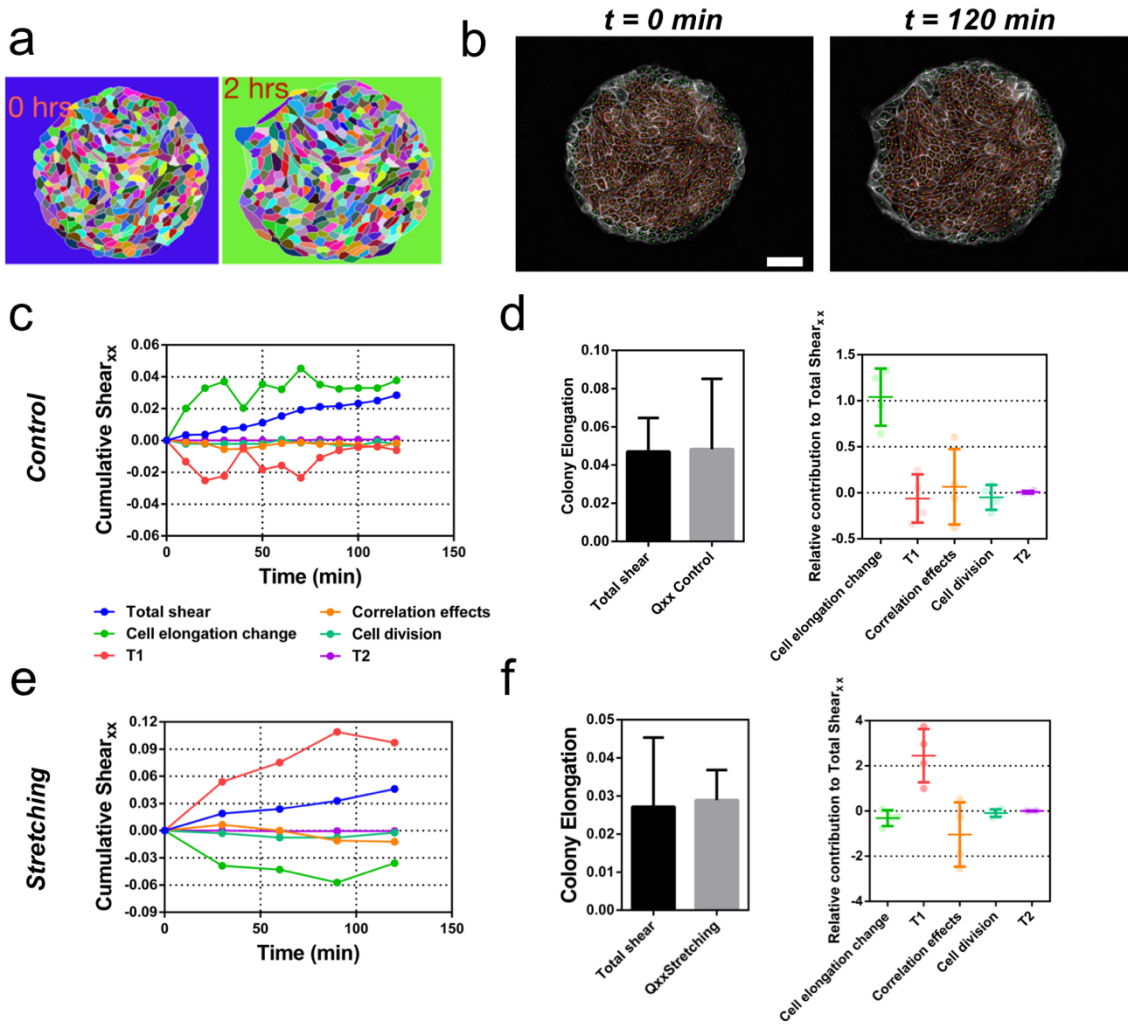

Figure 6. ***Contributions to symmetry breaking***. (**a**) Snapshots of two colonies from control condition segmented and tracked for cells using Tissue-Analyzer (TA) for a duration of $t = 120$ minutes starting from removal of stencil at $t = 0$. Scale bar 50 µm. (**b**) The segmented and tracked images are triangulated in Tissue-Miner (TM). Scale bar 50 µm. The green dots represent the centers of the segmented cells. (**c**) The dynamics of triangulation is analyzed in TM to provide the overall *xx* component of cumulative pure shear strain in a sample colony as a function of time (total shear). (**d**) Comparison between the mean total pure shear obtained from TM and the overall colony pure shear obtained from ellipse fitting (left). Total shear corresponds to $n_{colonies} = 4$ colonies from N = 2 independent experiments and Q_{xx} control was obtained from $n_{colonies} = 25$ colonies of N = 11 independent experiments. Relative contribution of the different processes to the total pure shear (right). Total shear and contributions were obtained from $n_{colonies} = 4$ colonies from N = 2 independent experiments. (**e**) Cumulative pure shear decomposition for stretched colony. (**f**) Comparison between the mean total pure shear obtained from TM and the overall colony pure shear obtained from ellipse fitting (left) and relative contribution of the different processes to the total pure shear (stretching case). Total shear corresponds to $n_{colonies} = 4$ colonies from N = 4 independent experiments and Q_{xx} stretching was obtained from $n_{colonies} = 20$ colonies of N = 9 independent experiments. Relative contribution of the different processes to the total pure shear (right). Total shear and contributions were obtained from $n_{colonies} = 4$ colonies from N = 4 independent experiments.

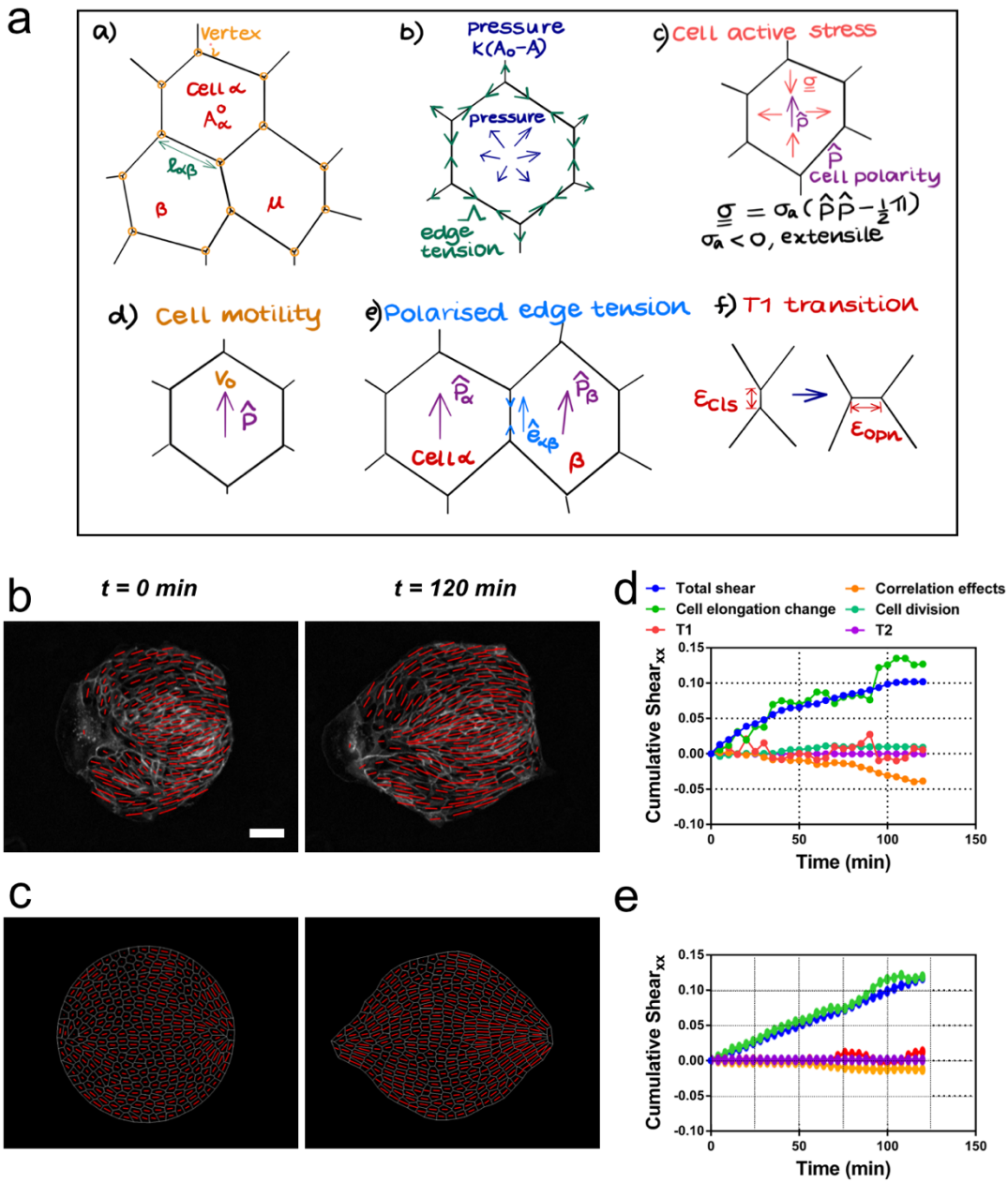

Figure 7. ***Vertex model recapitulates symmetry breaking and shear decomposition***. (**a**) Schematic of vertex model depicting the arrangement of cells, forcing, and topological transitions in a tissue. (a) 2-D monolayer of epithelial cells is represented by polygons, generally sharing a common edge and two vertices between cells. For any cell α shown in the figure, $A\alpha$ is the area, A_α^0 is the preferred area and $l\alpha\beta$ is the length of the edge shared between cells α and β. The forces on any vertex i in the basic vertex model are from (b) pressure due to deviation in the cell area from its preferred value and the tensile force arising from edge or cortical contractility Λ. In our model each cell also has a polarity $\hat{\boldsymbol{p}}$ associated with it through which active forces can act on the cell vertices due to (c) anisotropic cell active stress (extensile in our case), (d) cell motility v_0 and (e) polarised or biased edge tension that depends on the orientation of the edge $\hat{\boldsymbol{e}}_{\alpha\beta}$ with respect to the polarities of the adjoining cells. (f) When the edge connecting two cells becomes smaller than a critical value ϵ_{cls}, the cells are made to modify their neighbours by forming a new edge of length $\epsilon_{\text{opn}} > \epsilon_{\text{cls}}$ as shown. (**b**) Experimental coarse-grained cell shape nematic at *t=0* and *t=120* min. Scale bar 50 μm. (**c**) A vertex model with internal activity arising from extensile active cell stress and biased edge tension for the cell-cell junctions. (**d**) Overall *xx* component of cumulative

pure shear strain in the sample colony shown in (b) as a function of time (total shear). (**e**) Shear decomposition of the *in silico* experiment which is similar to its experimental counterpart in (**d**).

Supplementary Material

Epithelial colonies *in vitro* elongate through collective effects

Jordi Comelles[1], Soumya SS[2], S. Anvitha[3], Guillaume Salbreux[4], Frank Jülicher[5,6], Mandar M. Inamdar[2#], Daniel Riveline[1]*

- Figure Supplements
- Movie Captions
- Supplementary Information

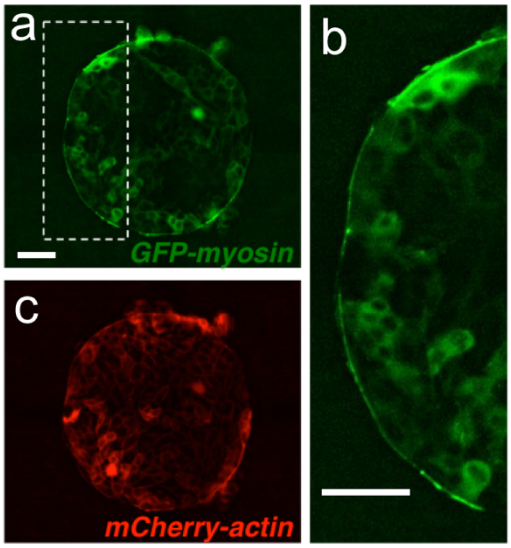

Figure 1 – figure supplement 1. ***A supra-cellular acto-myosin cable sets the boundary of the colony***. (**a**) MDCK cells expressing GFP-myosin. Scale bar 50 µm. (**b**) Inset of the myosin cable structure at t = 0 min. Small discontinuities in cable are visible. Scale bar 50 µm. (**c**) Image of the actin distribution for the same colony.

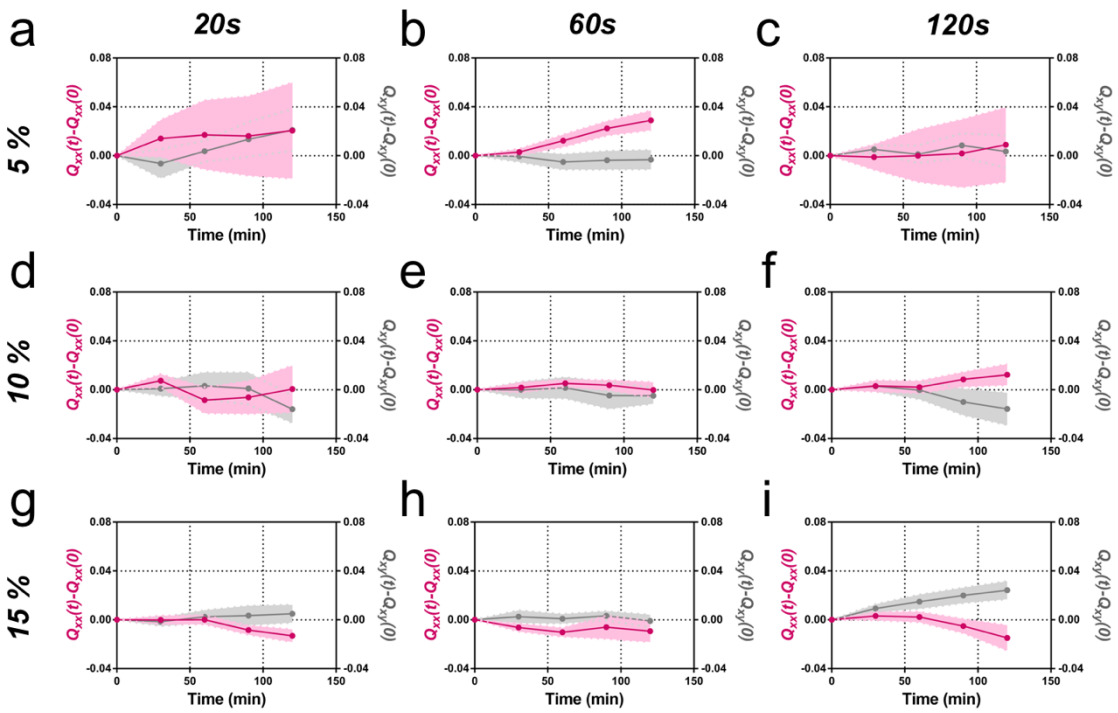

Figure 2 – figure supplement 1. ***Elongation as a function of frequency and amplitude of cyclic stretching***. Cumulative Q_{xx} (left y axis) and cumulative Q_{xy} (right y axis) during 120 min of colony expansion. Mean value ± standard error of the mean. (**a**) 5% amplitude and 20s frequency N = 3, n = 5 colonies. (**b**) 5% amplitude and 60s frequency N = 9, n = 20 colonies. (**c**) 5% amplitude and 120s frequency N = 5, n = 6 colonies. (**d**) 10% amplitude and 20s frequency N = 4, n = 6 colonies. (**e**) 10% amplitude and 60s frequency N = 5, n = 8 colonies. (**f**) 10% amplitude and 120s frequency N = 4, n = 8 colonies. (**g**) 15% amplitude and 20s frequency N = 3, n = 9 colonies. (**h**) 15% amplitude and 60s frequency N = 3, n = 6 colonies. (**i**) 15% amplitude and 120s frequency N = 3, n = 6 colonies.

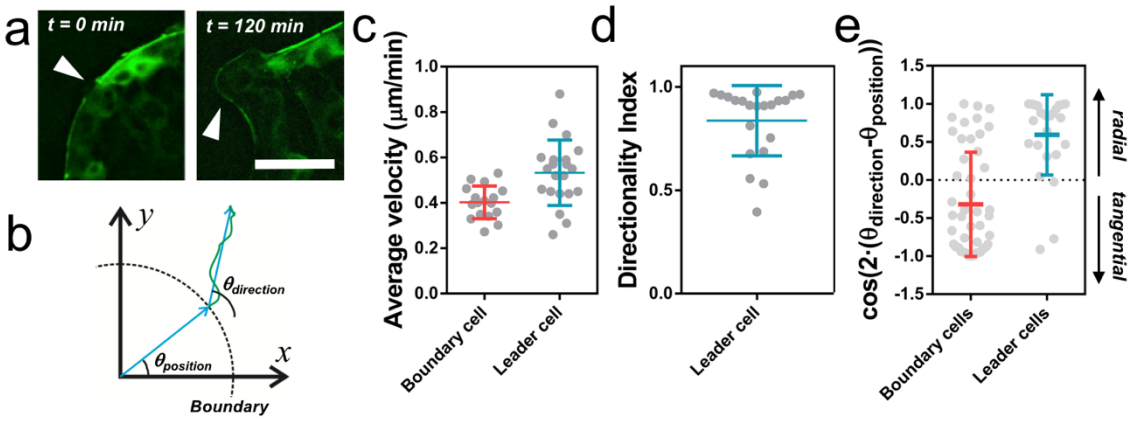

Figure 4 – figure supplement 1. ***Leader cell dynamics***. (**a**) Discontinuities in the myosin cable structure at t = 0 min (white arrows) become finger-like structures at t = 120 min (white arrows). Scale bar 50 μm. (**b**) Schematics of a cell trajectory. Its initial position at the boundary with respect to the center of the colony defines the angle $\theta_{position}$. The vector between the initial and the final position of the cell defines the trajectory direction $\theta_{direction}$. (**c**) Average velocity of cells at the outer rim of the colony. Leader cells are faster than other boundary cells. $n_{boundary}$ = 17 cells from 8 colonies and N = 4 independent experiments and n_{leader} = 21 cells from 12 colonies and N = 5 independent experiments. Individual cells in grey with Mean ± SD. (**d**) Directionality index for leader cells as the ratio of the distance between the initial and final position over the total distance covered by the cell. n_{leader} = 21 cells from 12 colonies and N = 5 independent experiments. Individual cells in grey with Mean ± SD. (**e**) Cosine of two times the angle difference between $\theta_{position}$ and $\theta_{direction}$ for cells at the boundary and cells in finger-like structures. Values close to 1 correspond to radial trajectories and values close to -1 correspond to tangential trajectories. Mean value ± standard deviation, $n_{boundary}$ = 49 cells from 8 colonies and N = 4 independent experiments and n_{leader} = 25 cells from 12 colonies and N = 5 independent experiments. Individual cells in grey with Mean ± SD.

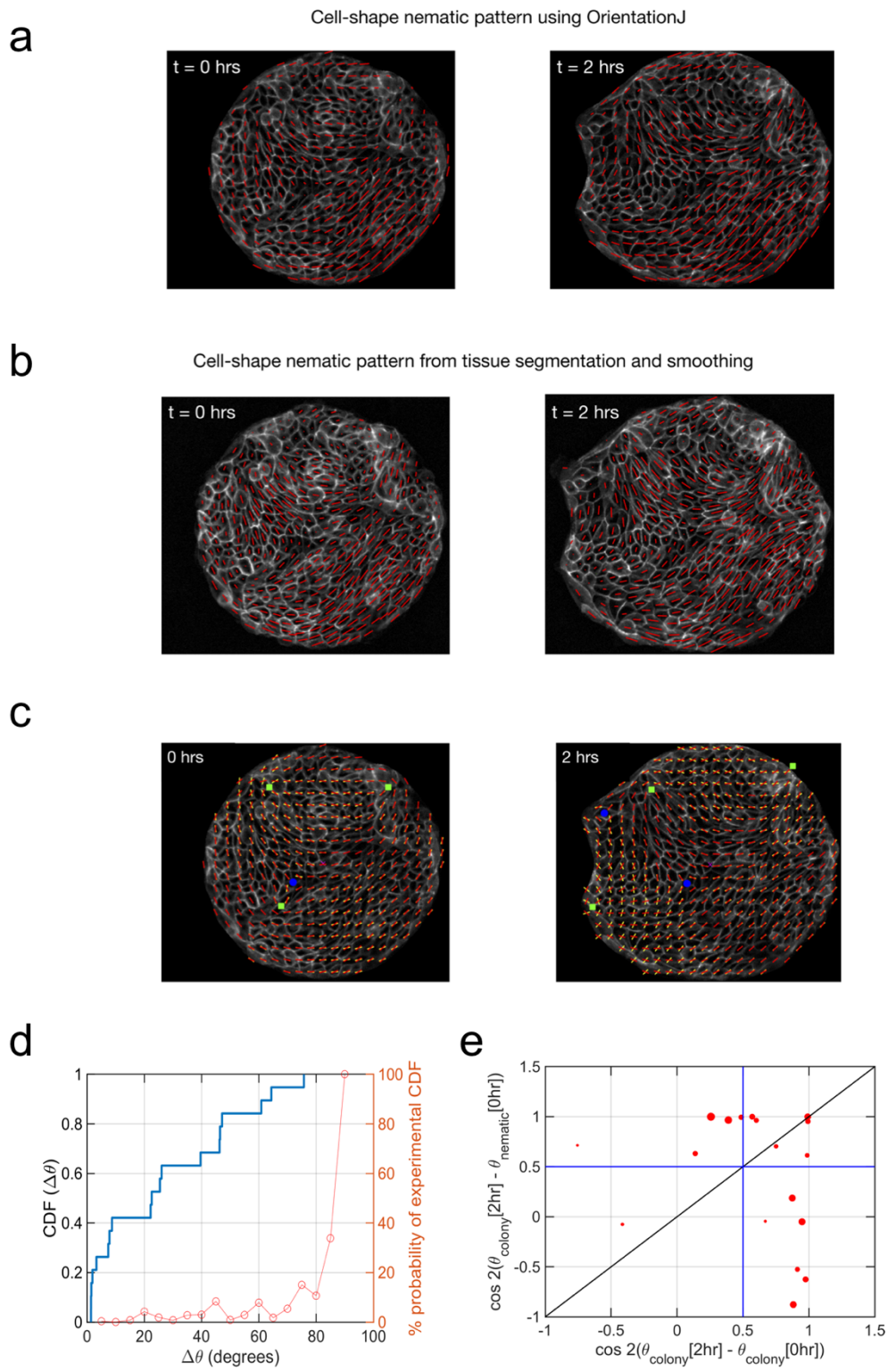

Figure 5 – figure supplement 1. ***Cell shape nematic field.*** Comparison of (**a**) cell shape nematic field obtained from OrientationJ plugin of ImageJ with (**b**) its counterpart obtained from tissue segmentation, triangulation and smoothing. It can be seen that the simpler, direct approach in (**a**) shows a very similar output as from the more detailed procedure in (**b**). (**c**) Fitting of cell-shape nematic field (yellow segments) with the one obtained experimentally (red segments) from OrientationJ using a simple expression (Eq. 14 of Supplementary Material) in terms of topological defects. The green squares and the blue circles represent, respectively, +1/2 and -1/2 topological defects at the corresponding locations obtained from the experimental nematic field. (**d**) Correlation between $\theta_{nematic}$ (0 hrs) and θ_{colony}(2 hrs) for finite sample size. Simple calculation to

obtain the probability of observing a cumulative distribution function (CDF) for $\Delta\theta$, the angle between the mean colony shape nematic $\theta_{nematic}$ at 0 hrs and overall colony elongation θ_{colony} at 2 hrs, in the absence of any physical correlation between these two quantities, i.e., $\Delta\theta$ is picked with uniform probability from the set [0°, 90°] (orange curve and y axis on the right). It can be seen that in such a case, the probability to experimentally observe CDF > 0.6 for $\Delta\theta = 30°$ in a sequence of 19 independent experiments is less than 1/100. This provides a strong indication that $\theta_{nematic}$(0 hrs) is very likely to be physically connected with θ_{colony}(2 hrs) and not randomly picked between 0° and 90°. n = 19 colonies of N = 5 independent experiments. (**e**) Final orientation of the colony is correlated with the initial shape nematic of initial orientation. The orientation of mean cell shape nematic $\theta_{nematic}$ of the colony at 0 hrs is strongly correlated with the overall orientation of the colony θ_{colony} at 2 hrs as can be inferred from the presence of 12 out of 19 experiments above the horizontal blue line at 0.5 (corresponding to $\Delta\theta = 30°$). Of the rest of the 7 colonies which do not show this trend, 6 colonies show a strong correlation of their final orientation with their orientation at the start of experiment. The size of the red circles is proportional to the magnitude of anisotropy of the colony shape after 2 h. n = 19 colonies of N = 5 independent experiments.

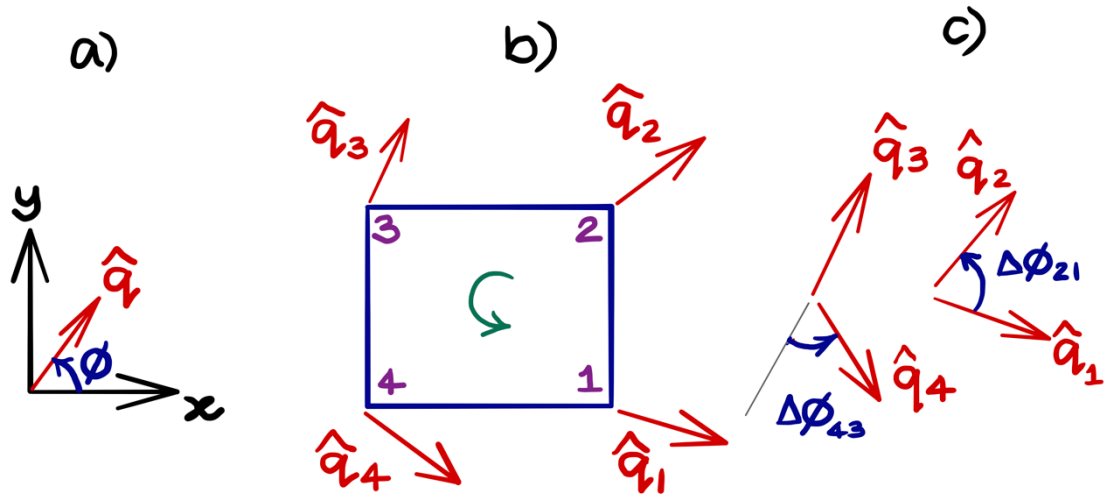

Figure 5 – figure supplement 2: Obtaining topological charge for the orientation field $\hat{q}$ on a rectangular grid. (**a**) An orientation director $\hat{\boldsymbol{q}} = \cos\phi\,\hat{\boldsymbol{e}}_x + \sin\phi\,\hat{\boldsymbol{e}}_y$ makes an angle ϕ with the axis as shown. (**b**) The orientation field at the nodes of the smallest cell of the rectangular grid. The topological charge of $\hat{\boldsymbol{q}}$ within the cell is obtained by calculating the change in the orientation angle $\Delta\phi$ between the adjacent nodes of the grid and traversed in the anticlockwise direction. (**c**) The angle $\Delta\phi$ is taken to be the smallest of the angles between the adjacent directors and respects the nematic nature (or $\hat{\boldsymbol{q}}$ and $-\hat{\boldsymbol{q}}$ symmetry) of the field. We note that this procedure is ambiguous when $\Delta\phi$ is a multiple of π/2, a case that generally does not happen in practice. After using anticlockwise $\Delta\phi > 0$ and clockwise $\Delta\phi < 0$, the net topological charge of the orientation field $\hat{\boldsymbol{q}}$ within the rectangular cell in (b) is obtained as $k = \frac{1}{2\pi}\sum_j \Delta\phi_{j+1,j}$.

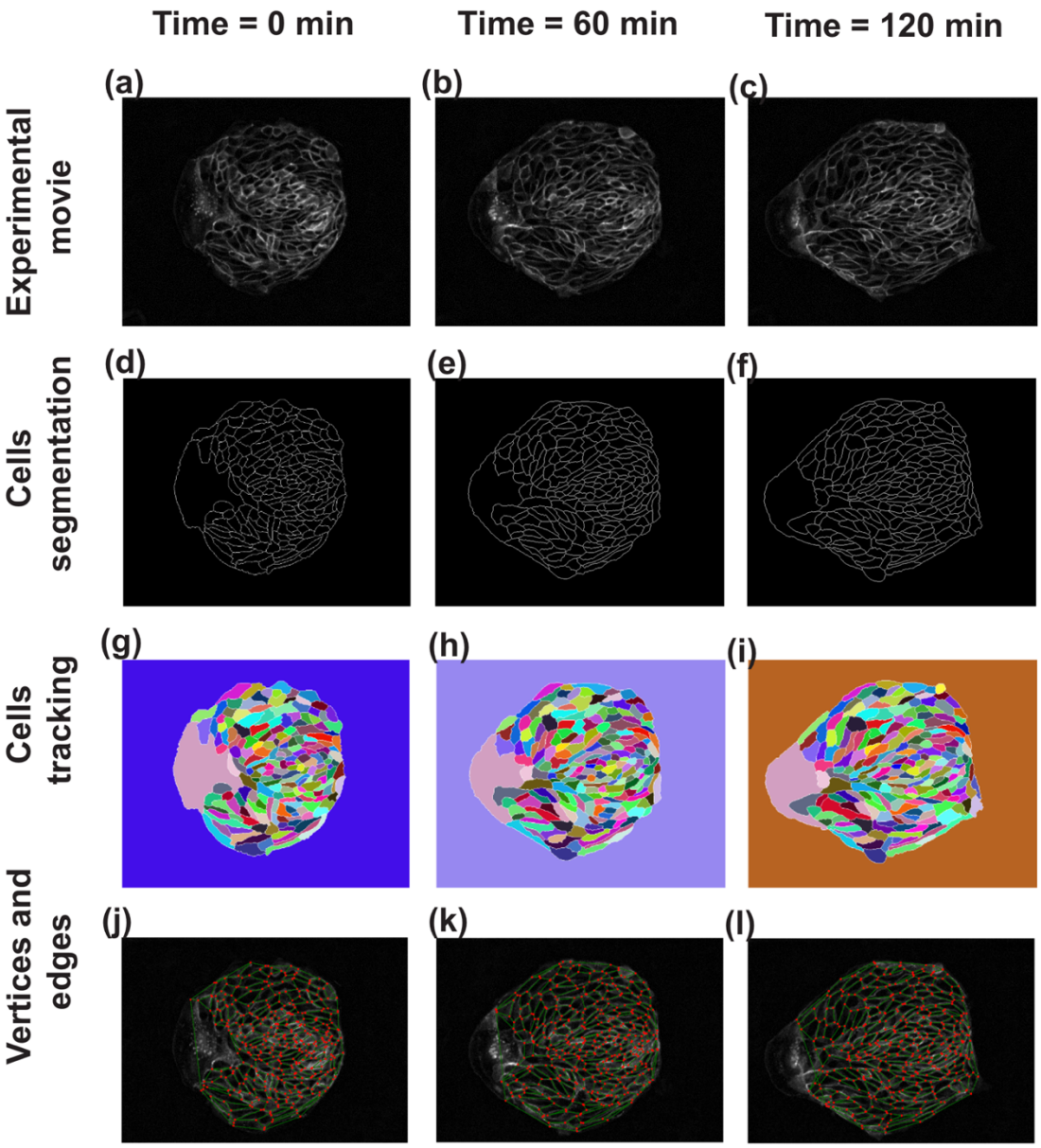

Figure 6 – figure supplement 1. ***Steps in image analysis.*** As the first step of analysis using TissueMiner, the images obtained from the experiment have been skeletonized, segmented and tracked using TissueAnalyser. (**a**–**c**) Show the images of cell colony at three different time points. (**d**–**f**) In order to differentiate the cell edges from the rest of the tissue for easy edge detection, the tissue has been skeletonized by adjusting the threshold value. (**g**–**i**) TissueAnalyser detects the edges and segments the colony, based on a watershed algorithm. At this step, algorithm also tracks the cells and assigns them a color and a global track identity, which remain constant throughout the process. When a cell undergoes division, a new track identity and color are assigned to one of the two daughter cells, while keeping the other same. (**j**–**l**) Using the output from TissueAnalyser, TissueMiner analyzes the tissue and represents it as a collection of cells made of a network of edges (green lines) connected to vertices (red dots) at any given time.

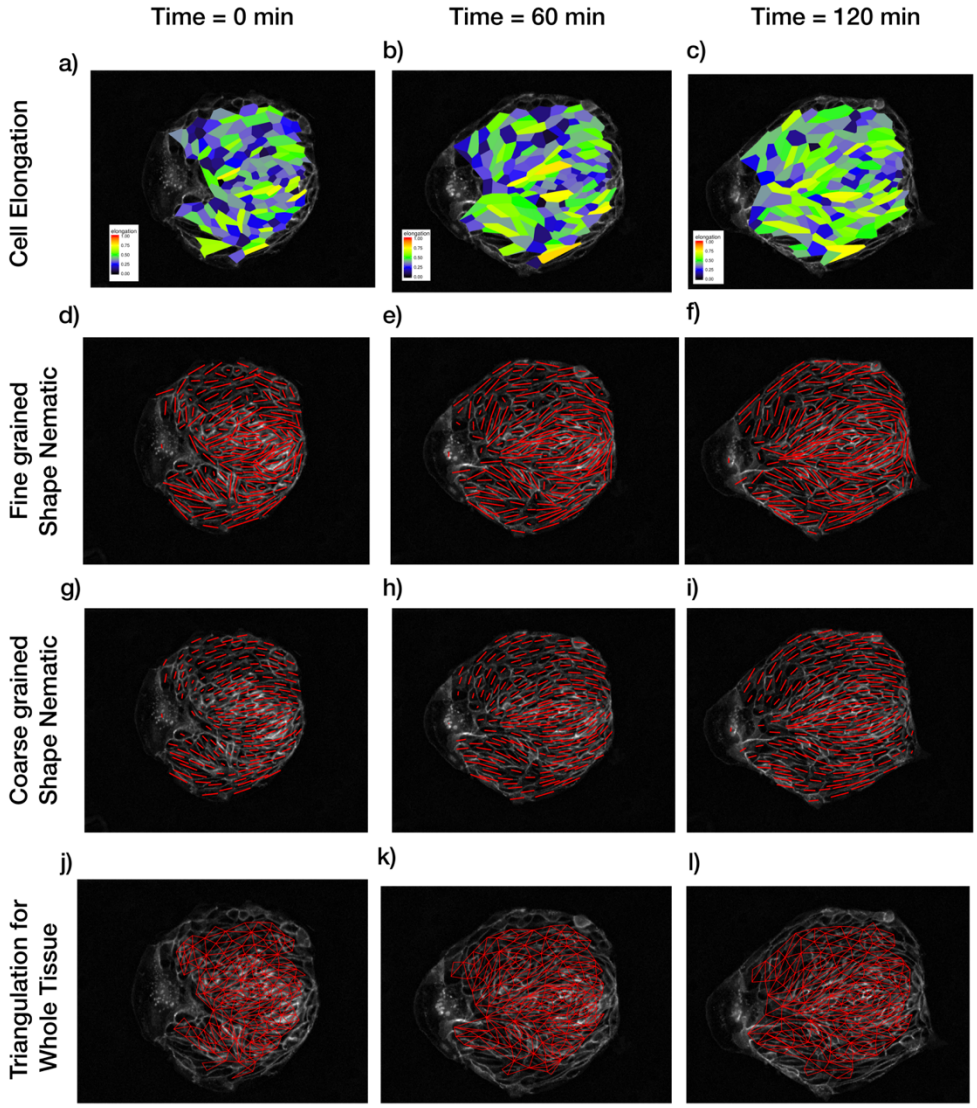

Figure 6 – figure supplement 2. ***Patterns of cellular parameters obtained from TissueMiner*** **analysis.** (**a** – **c**) Cell elongation magnitude distribution is plotted for three different time points. (**d** – **f**) Actual fine-grained cell elongation nematic for individual cells. The length of the segments is proportional to the magnitude of cell-shape nematic ε and the orientation is φ (see Supplementary Material Section V) (**g** – **i**) Coarse-grained cell shape nematic is obtained by using a Gaussian kernel of size 30 pixels around every cell. (**j** – **l**) The algorithm to find out tissue deformation is based on the triangulation method as described in Refs. [23, 27] of the main paper. Any topological changes in the form of T1 transition, cell division or cell extrusion will lead to a new triangulation. The triangulation is not reliable near the boundary and hence a layer of cells near the boundary is not included in the triangulation and subsequent calculations for tissue pure shear.

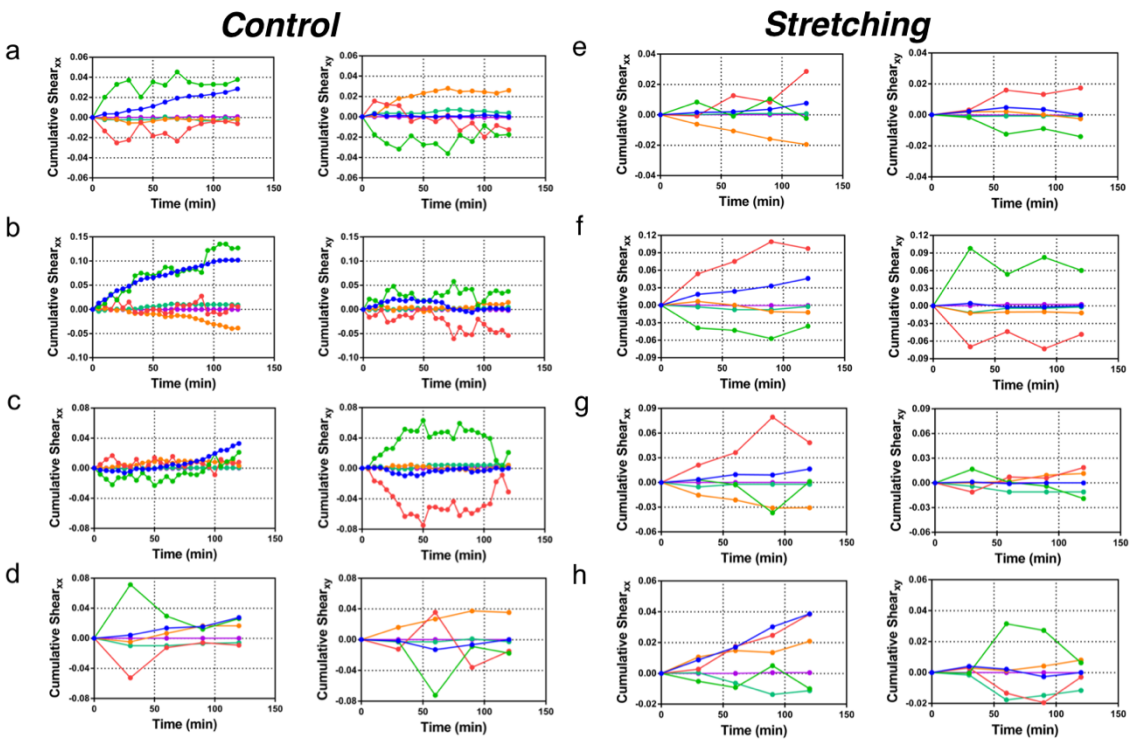

Figure 6 – figure supplement 3. ***Cumulative pure shear decomposition.*** (**a-d**) Control experiments. Decomposition of pure shear (blue) into its components arising from cell shape change (green), T1 transitions (red), correlation effects (orange), cell division (turquoise), and cell extrusion (purple). The *x* direction for each colony is chosen such that *xy* component of total shear is zero at t = 120 mins, and indicates the overall orientation of colony anisotropy. The anti-correlation effect between cell elongation and other components that is seen in Fig. 4f of the main paper is clearly visible in every case. The interval between subsequent time data points is 10 min for (**a**), 5 mins in (**b-c**) and 30 mins for (**d**). The data for *xx* component of pure shear in (**a**) is presented in Figure 6. (**e-h**) Stretched colonies. Same analysis method and time evolution of pure shear presented in (**a-d**) for control colonies, but now for stretched colonies. The time interval between subsequent time data points is 30 mins. Interestingly, the anti-correlation effect between the cell elongation and other components with respect to the total pure shear is seen here too.

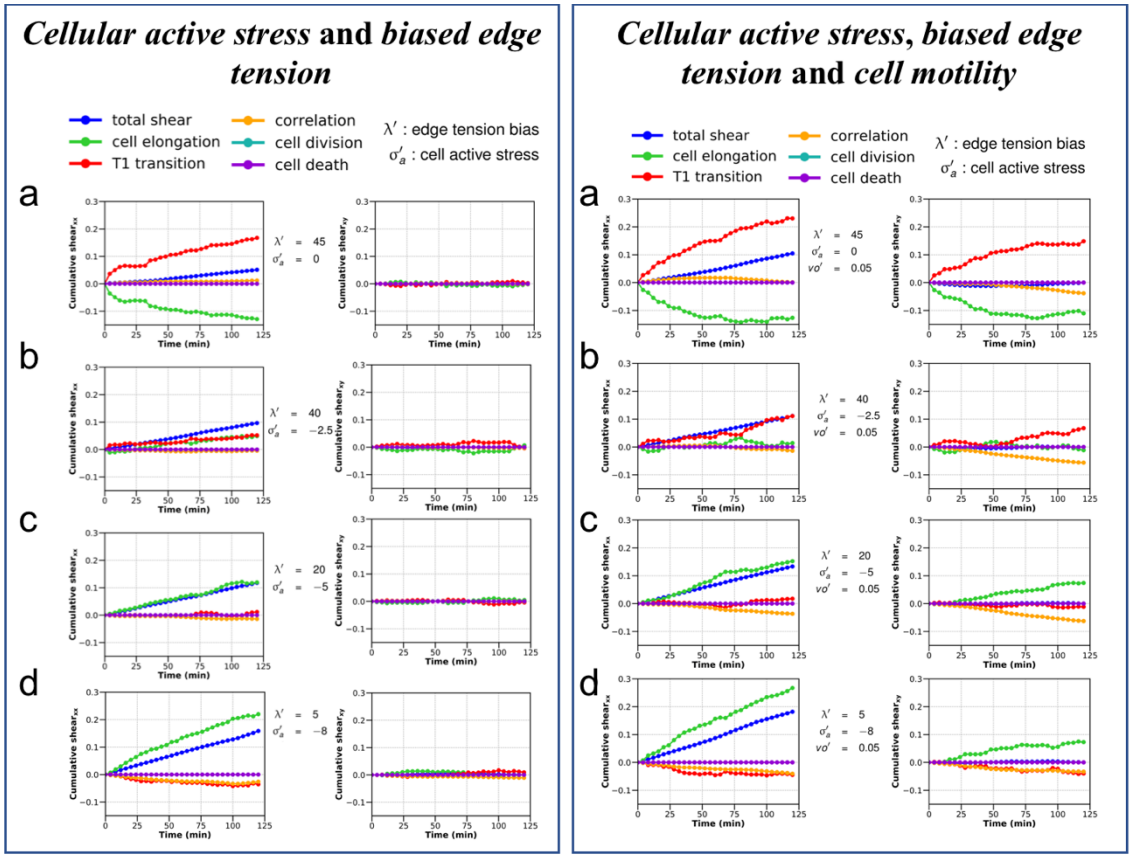

Figure 7 – figure supplement 1. ***Cumulative pure shear decomposition patterns for the simulated colonies.*** (**Left**) Varying strength of cellular active stress and biased edge tension. Briefly, the *cellular active stress* (σ_a') is an internal cellular stress that tends to drive cell elongation. Biased edge tension (λ') is implemented by modulating the line tension of the cell edges on the basis of the relative angle the edges makes with the polarity of their two shared cells. A colored noise with a small strength and persistence time is applied on the edge line tension to ensure baseline fluctuations. Note the relative positions of the pure shear due to T1 transitions (red) and cell elongations (green) with respect to the overall colony shear (blue). The *x* axis is chosen to be the major axis of elongation such that the *xy* component of cumulative total pure shear strain is zero at the end of the simulation. It can be seen from a-d that the relative position of the red and green curves with respect to the blue curve is an indication of the internal processes which are more dominant in a particular colony and show marked similarity with the corresponding experimental curves seen in Figure 6 – figure supplement 1. (**Right**) Varying strength of *cellular active stress*, *biased edge tension* and *cell motility.* All simulations shown here are as in left panel a-d, but with the addition of a small motility term v_0'. It can be clearly seen that addition of motility does not qualitatively modify the relative positions of the contributions from cell elongation (green) and T1 transitions (red) with respect to each other when compared with their counterparts in left panel. However, in this particular case, for the parameters and the initial conditions, the *xy* component of the shear is comparatively more dominant.

Movie 1. **Spontaneous symmetry breaking of circular colonies**. Time-lapse of a MDCK cells colony freely evolving after removal of a PDMS stencil. Time in hh:mm. Scale bar 50 µm.

Movie 2. **Cyclic stretching of MDCK colonies**. Time-lapse of a MDCK colony under cyclic stretching (5% and 120s). Time in hh:mm:ss. Scale bar 50 µm.

Movie 3. **Expansion of MDCK colonies under cyclic stretching**. Time-lapse of a MDCK colony under cyclic stretching (5% and 60s) at the 0% strain position. Time in hh:mm. Scale bar 50 µm.

Movie 4. **Early symmetry breaking of circular colonies**. Composite array time-lapse of MDCK-GFP-Ecadherin cells colonies during the first two hours of expansion. Time in hh:mm. Scale bar 50 µm.

Movie 5. **Nematic field alignment precedes colony elongation**. Movie showing cell-shape nematics and topological defects of an elongating colony. Time in hh:mm. Scale bar 50 µm.

Movie 6. **Contributions to colony elongation**. Movie showing cell tracking, neighbor triangulation, cell-shape nematics and topological defects of an elongating colony. Time in hh:mm. Scale bar 50 µm.

Movie 7. ***In silico* recreation of a colony elongation**. Vertex model simulation of a colony elongation. Cell-shape nematics, topological defects and cell polarization are followed over time.

Supplementary Information: Comelles et al.

I. QUANTIFICATION OF TISSUE KINEMATICS

In the first step of analysis, time-lapse images of MDCK colonies are segmented to partition the tissue into individual cells and then tracked for their movements using Tissue-Analyser (TA) plugin of FIJI [1, 2] (see Figure 6 – figure supplement 1a-i). This information of the tracked cell colony is then passed to Tissue-Miner (TM), which extracts data and stores the cellular geometry and connectivity in the form of cell vertices and bonds using a *snakemake* based automated workflow (see Figure 6 – figure supplement 1j-l). As described in Refs. [3, 4], TM has *R* or *Python* API that can be used to quantify fine-grained (cell-level) and coarse-grained (colony-level) deformation properties of epithelial colonies. Even though the scripts to calculate the basic kinematic quantities are available, users have the freedom to add new computational routines to calculate the quantities of their interest.

A. Analysis of cell elongation

Cell-shape anisotropy is an important marker of stress in the cells in response to either internal activity or external forcing [5, 6]. To understand and quantify the elongation of cells over time, TM computes an elongation parameter proposed in Ref. [1]. In their study to understand the role of flow in orienting the axis of polarity in *Drosophila* wings, Aigouy et al. [1] use a nematic tensor with a magnitude and orientation to quantify the elongation of each cell. For a given cell with area A_c, the elongation nematic tensor is proposed as

$$E = \begin{bmatrix} \epsilon_{xx} & \epsilon_{xy} \\ \epsilon_{xy} & -\epsilon_{xx} \end{bmatrix}. \tag{1}$$

This tensor E is traceless and symmetric with components given by

$$\begin{aligned} \epsilon_{xx} &= \frac{1}{A_c}\int_0^{2\pi}\int_0^{R(\phi)} \cos(2\phi) r dr d\phi \\ \epsilon_{xy} &= \frac{1}{A_c}\int_0^{2\pi}\int_0^{R(\phi)} \sin(2\phi) r dr d\phi \end{aligned}, \tag{2}$$

where $R(\phi)$ is the distance to cell boundary at an angle ϕ (SI of Ref. [1]). For this nematic tensor, the magnitude is given by

$$\epsilon = ({\epsilon_{xx}}^2 + {\epsilon_{xy}}^2)^{\frac{1}{2}}, \tag{3}$$

and the orientation is given by angle ϕ

$$\begin{aligned} \cos(2\phi) &= \frac{\epsilon_{xx}}{\epsilon}, \\ \sin(2\phi) &= \frac{\epsilon_{xy}}{\epsilon}. \end{aligned} \tag{4}$$

Based on the above expressions, the spatial distribution of the magnitude of shape nematic for individual cells within the colony for three time points is shown in Figure 6 – figure supplement 2a-c. The fine-grained nematic segments for individual cells whose magnitude is proportional to ϵ and orientation is ϕ (Figure 6 – figure supplement 2d-f). The coarse-grained representation of this tensor (Figure 6 – figure supplement 2g-i) is obtained by spatially averaging the elongation nematic over several cells by using a Gaussian smoothing kernel of size comparable to the size of cells (30 pixels in this case). From the figures it is clear the elongation of interior cells is strongly correlated with the orientation of the future 'finger' even at $t = 0$ h.

B. Analysis of tissue deformation from components of pure shear strain via triangulation

As discussed earlier, during different stages of morphogenesis, epithelial tissues are reported to undergo a series of physical changes. The various internal and external forces that are being applied to the tissue during these processes

result in deformation and rearrangement of constituent cells. The shape modification rate of the tissue is quantified in terms of the anisotropic component of shear strain rate. However, at the tissue level in epithelial sheets, shear strain can arise due to a combination of cell elongation, T1 transitions, cell division, cell extrusion, and correlation effects. By studying each both component separately and with respect to the other components, one can get hints regarding the mechano-chemical state of the colony. As is described in Ref. [4], for any general 2-D velocity vector $\mathbf{v}$, the gradient tensor can be defined as

$$v_{ij} = \partial_i v_j = \begin{bmatrix} \frac{\partial v_x}{\partial x} & \frac{\partial v_y}{\partial x} \\ \frac{\partial v_x}{\partial y} & \frac{\partial v_y}{\partial y} \end{bmatrix}. \tag{5}$$

The above velocity gradient tensor for a group of cells can be split into three parts: (i) isotropic component to obtain the rate of area change, (ii) symmetric traceless component to quantify the pure shear strain rate, and (iii) an antisymmetric part that represents the local vorticity [4, 7] as follows

$$\begin{aligned} v_{ij} &= \frac{1}{2} v_{kk}\delta_{ij} + \tilde{v}_{ij} + \omega\delta_{ij} \\ &= \underbrace{\frac{1}{2}\begin{bmatrix} \frac{\partial v_x}{\partial x} + \frac{\partial v_y}{\partial y} & 0 \\ 0 & \frac{\partial v_x}{\partial x} + \frac{\partial v_y}{\partial y} \end{bmatrix}}_{v_{kk}\text{:isotropic}} + \underbrace{\frac{1}{2}\begin{bmatrix} \frac{\partial v_x}{\partial x} - \frac{\partial v_y}{\partial y} & \frac{\partial v_y}{\partial x} + \frac{\partial v_x}{\partial y} \\ \frac{\partial v_y}{\partial x} + \frac{\partial v_x}{\partial y} & \frac{\partial v_y}{\partial y} - \frac{\partial v_x}{\partial x} \end{bmatrix}}_{\tilde{v}_{ij}\text{:symmetric, anisotropic}} + \underbrace{\frac{1}{2}\begin{bmatrix} 0 & \frac{\partial v_y}{\partial x} - \frac{\partial v_x}{\partial y} \\ \frac{\partial v_x}{\partial y} - \frac{\partial v_y}{\partial x} & 0 \end{bmatrix}}_{\omega\text{:antisymmetric}}. \end{aligned} \tag{6}$$

Here, more specifically, $v_{kk} = v_{xx} + v_{yy}$ is the trace of the velocity gradient tensor, or the divergence of the velocity field and quantifies the rate of contraction or expansion in the cell area. The traceless symmetric part $\tilde{v}_{ij}$ is the pure shear strain rate and quantifies shape changes in the tissue. The antisymmetric component ω is the vorticity of the velocity field and provides values of rotational rates of the group of cells during deformation.

The total pure shear strain rate of the tissue $\tilde{v}_{ij}$, now represented in a tensorial form $\tilde{\mathbf{V}}$, can be further split into traceless, symmetric, components as follows

$$\tilde{\mathbf{V}} = \frac{D\mathbf{Q}}{Dt} + \mathbf{T} + \mathbf{C} + \mathbf{E} + \mathbf{D}, \tag{7}$$

where $\mathbf{Q}$ is the shear contribution coming from average cell elongation, $\mathbf{T}$ is the shear contribution from T1 transitions, $\mathbf{C}$ from cell divisions, $\mathbf{E}$ from cell extrusions and $\mathbf{D}$ due to the correlations effects in the tissue which arise due to coarse graining effects. Detailed derivation and discussion of this expression are available in Refs. [3, 4, 7]. The contributions from above mentioned components are quantified using the triangulation approach [3]. As shown in Figure 6 – figure supplement 2j-l, the triangulation method considers the entire colony without the boundary cells as a network of triangles, connecting the centers of the neighboring cells. Any topological changes in the form of cell division or extrusion will lead to a new triangulation. The shear strain rates in Eq. 7 can be integrated over time to provide cumulative shape deformation and the corresponding cumulative shear decomposition for the cell colony, and is obtained for the complete colony without including the external boundary cells (Figure 6b). Figure 4 of Ref. [7] schematically represents this decomposition of total tissue shear into individual cellular events.

In *Drosophila* pupal wing the x axis is naturally provided by the A-P axis. In our *in vitro* situation, however, the x axis is chosen as the dominant direction of colony elongation, such that at the end of the experiment ($t = 2$ h) the cumulative value of the total shear strain rate $\tilde{v}_{xy} = 0$. The cumulative shear decomposition plots for the experiments and simulations are shown in Figure 6b and Figure 6 – figure supplement 3 and Figure 7 – figure supplement 1.

C. Correlation between the orientation of mean cell-shape nematic and the orientation of the overall colony elongation

As discussed earlier, the shape of a cell can be thought of to be represented by a nematic tensor $\mathbf{Q}^{\text{cell}}$. Upon averaging this quantity over multiple cells, we obtain nematic field $\mathbf{Q}^{\text{nem}}(x, y, t)$ over the colony. As described in the previous sub-section, this nematic tensor is traceless and symmetric with an orientation $\phi(x, y, t)$ (Figure 5 – figure supplement 1 and Figure 6 – figure supplement 2g-i) and magnitude $Q^{\text{nem}}(x, y, t)$ such that

$$Q^{\text{nem}}_{xx}(x, y, t) = Q^{\text{nem}} \cos 2\phi \text{ and} \tag{8}$$

$$Q^{\text{nem}}_{xy}(x, y, t) = Q^{\text{nem}} \sin 2\phi. \tag{9}$$

This nematic field is obtained for our MDCK colonies by analyzing time-lapse images with the OrientationJ plugin of ImageJ [8, 9]. We verified that this image based approach gives results that are comparable with those obtained by

spatially smoothing (with Gaussian kernel) the individual cell-shape nematics extracted from the segmented images of the colonies (Supplementary Material Section IA, Figure 5 – figure supplement 1 and Figure 6 – figure supplement 2). At any particular time t, the mean nematic field for the colony is

$$Q_{xx}^{\mathrm{ncol}}(t) = \langle Q_{xx}^{\mathrm{nem}}(x,y,t)\rangle_{x,y} \text{ and} \tag{10}$$

$$Q_{xy}^{\mathrm{ncol}}(t) = \langle Q_{xy}^{\mathrm{nem}}(x,y,t)\rangle_{x,y}. \tag{11}$$

The orientation of the mean cell-shape nematic is then simply

$$\theta_{\mathrm{nematic}}(t) = \frac{1}{2}\tan^{-1}\left(\frac{Q_{xy}^{\mathrm{ncol}}(t)}{Q_{xx}^{\mathrm{ncol}}(t)}\right), \tag{12}$$

where $\tan^{-1}$ is implemented in Matlab using the inbuilt function `atan2` [10]. In this analysis, the *coherence* of the image structure tensor is the counterpart of Q^{col}, the magnitude of the mean cell-shape nematic [8]. We then compare the final colony orientation $\theta_{\mathrm{colony}}(t = 2 \text{ hrs})$, which is obtained from ellipse fitting, with the orientation of the mean colony nematic $\theta_{\mathrm{nematic}}(t = 0 \text{ hrs})$ (Figure 5b and Figure 5 – figure supplement 1). Also refer to Materials and Methods: Orientation field of the cells and topological defects in the Main Paper for additional details.

D. Topological defects as readouts of cell-shape nematic orientation field

Any nematic field can contain topological defects [11]. A visual inspection of the cell-shape orientation field $\mathbf{q} = \cos\phi\hat{\mathbf{e}}_x + \sin\phi\hat{\mathbf{e}}_y$ for MDCK colonies indicates the possible presence of topological defects (Figure 5 and Figure 5 – figure supplement 1). The strength k of topological charge for this field (Supplementary Section IC) in a given region is obtained as

$$k = \frac{1}{2\pi}\oint \frac{d\phi}{ds}ds, \tag{13}$$

where the line integral is calculated by traversing the curve that encloses this region in an anticlockwise sense. For the experimental colonies, the nematic field is not continuous but obtained on the vertices of the grid-cell as shown in Figure 5 – figure supplement 2. In this case, the topological charge k enclosed within the grid-cell is

$$k = \frac{1}{2\pi}\sum_j \Delta\Phi_{j+1,j}, \tag{14}$$

where the notation is as shown in Figure 5 – figure supplement 2. If no topological defect is present within the cell then $k = 0$. Else, the net topological charge would evaluate to $k = \pm 1/2$, corresponding to the effective strength of the topological defects within the cell.

The location and strength of topological defects thus obtained for the experimental data could then be used to approximately depict the entire nematic field as follows. We first model the energetics of the nematic orientation field with one constant Frank free energy [12]. If we then assume that the orientation field ϕ is in local mechanical equilibrium at every time-step, it will then satisfy the Laplace equation $\nabla^2\phi = 0$ [11]. The resulting orientation field $\phi(x,y)$ for the nematic field in the presence of a single topological defect of strength k at the origin has a singular solution of the form

$$\phi = A\theta + \alpha, \tag{15}$$

where θ is the polar angle and α is a harmonic function that satisfies that Laplace equation [11]. However, for the current paper we find that taking α to be a constant that determines the orientation of the topological defect is sufficient to approximate the orientation nematic field (Figure 5d). Hence, as per Eqs. 13 and 15 the integral

$$\oint d\phi = 2\pi k, \tag{16}$$

for a closed curved around the defect gives $A = k$. If multiple defects are present in the domain, this solution for ϕ can be generalised to give

$$\phi_\alpha(x,y) = \alpha + \sum_i k_i \underbrace{\tan^{-1}\left(\frac{y-y_i}{x-x_i}\right)}_{\theta \text{ for defect } i}, \tag{17}$$

where $\{x_i, y_i\}$ and k_i are the coordinates and the strength, respectively, of the ith nematic topological defect obtained from the experimental data, and α dictates the orientation of the defect. Here, the subscript α in $\phi_\alpha(x, y)$ is added to distinguish it from the experimentally obtained $\phi(x, y)$. As before, $\tan^{-1}$ is implemented in Matlab using the inbuilt function `atan2` [10]. We now use the fitting parameter α in $\phi_\alpha(x, y)$ to see how well it represents the orientation field $\phi(x, y)$ by using the following procedure. The experimental field is obtained on a grid with N points $\{x_k, y_k\}$, where $k = 1, \ldots, N$. The difference between ϕ and ϕ_α is quantified by the residue

$$r_\alpha = -\frac{1}{N}\sum_{k=1}^{N}\cos^2(\phi^k - \phi_\alpha^k) \tag{18}$$

obtained over the grid points k. The minimization of the value of r_α over α would provide us with a field where $\phi \approx \phi_\alpha$ in a mean sense. Interestingly, by using this simple approach with just one fitting parameter α, we can get an excellent representation of the experimentally obtain nematic orientation field $\hat{\mathbf{q}}$ (Figure 5d).

E. Statistical test for cumulative distribution of the orientation differences between $\theta_{\text{nematic}}(0\text{ hrs})$ and $\theta_{\text{colony}}(2\text{ hrs})$

To check if the orientation of the colony elongation at $t = 2$ hrs is correlated with the orientation of the mean cell-shape nematic at $t = 0$ hrs, we examine the difference $\Delta\theta = |\theta_{\text{colony}}(2\text{ hrs}) - \theta_{\text{nematic}}(0\text{ hrs})|$. Specifically, as shown in Figure 4c, we obtain the cumulative distribution function (CDF) for $\Delta\theta$. If the quantity $\Delta\theta$ is completely random, i.e., $\theta_{\text{colony}}(2\text{ hrs})$ is completely uncorrelated with $\theta_{\text{nematic}}(0\text{ hrs})$, then the probability density for $\Delta\theta \in [0°, 90°]$ is equal to $1/90°$. In such a case the CDF($\Delta\theta$) as a function of $\Delta\theta$ should simply be a straight line with a slope of $1/90°$. However, it can clearly be seen that the experimentally observed CDF is significantly above this line, especially at relatively smaller values of $\Delta\theta \leq 30°$. This indicates that there indeed is correlation between $\theta_{\text{colony}}(2\text{ hrs})$ and $\theta_{\text{nematic}}(0\text{ hrs})$.

We now note that the total number of experiments (colonies) that were analysed for Figure 4c is $N = 19$. To check if the correlation between $\theta_{\text{colony}}(2\text{ hrs})$ and $\theta_{\text{nematic}}(0\text{ hrs})$ holds up for this finite sample size, we do the following. Let us take the probability density $p(\Delta\theta) = 1/90°$, $\forall\Delta\theta \in [0°, 90°]$, i.e., this relative angle $\Delta\theta$ is uniformly random between 0° and 90°. If we now sample $N = 19$ values for $\Delta\theta$ then we have created a *random* counterpart to the actual experimental result. We repeat this trial using a straightforward Matlab script and obtain $M = 10^6$ samples, each with $N = 19$ experiments. Of all the samples thus randomly generated, for a given $\Delta\theta$ we select those samples i for which $\text{CDF}_{\text{i}}^{\text{random}}(\Delta\theta) \geq \text{CDF}^{\text{experiment}}$. If for a particular $\Delta\theta$ the total number of such selected samples is $m(\Delta\theta)$, the probability of observing equal or higher bias towards alignment of the two angles from a random experiment than that actually observed experimentally is $P(\Delta\theta) = m(\Delta\theta)/M$ (Figure 5 – figure supplement 1d). It can clearly be seen that the percentage probability of observing such high values of CDF for smaller $\Delta\theta < 30°$ from a completely random sampling of $\Delta\theta$ is ≈ 1, i.e., approximately one sample of $N = 19$ experiments for every 100 samples, a very low number. The few colonies for which $\theta_{\text{nematic}}(0\text{ hr})$ does not match well with $\theta_{\text{colony}}(2\text{ hr})$ appear to align with the orientation $\theta_{\text{colony}}(0\text{ hr})$ of tissue initial elongation – the associated mechanism is, however, still open (see Figure 5 – figure supplement 1e). This entire analysis clearly indicates that the orientation of the mean cell-shape nematic at the initial time has correlation with the final anisotropy orientation of the colony with a high probability.

II. VERTEX MODEL SIMULATION

A planar vertex model is one of the most commonly used computational tool to understand mechanics of epithelial monolayers [13]. In this description, the tissue is assumed to be a 2-D sheet composed of cells which are represented by planar polygons sharing vertices and edges with their neighbors (Figure 7a). Governing equations are formulated to study the dynamics of evolution of each vertex of a cell. The total effective *energy* or work-function W of the tissue arises from area deformation of the cells and a combination of acto-myosin contractility and membrane adhesion energy at the cell interfaces (Figure 7b).

$$W = \sum_{\alpha=1}^{N}\frac{K_\alpha}{2}(A_\alpha - A_\alpha^0)^2 + \sum_{<\alpha\beta>}\Lambda_{\alpha\beta}l_{\alpha\beta}, \tag{19}$$

where for a particular cell α, A_α is the actual area and A_α^0 is the preferred cell area. $l_{\alpha\beta}$ is the length of the bond connecting shared between the cells α and β and $\Lambda_{\alpha\beta}$ is the effective contractility of that bond [14]. Note that the energy W depends both on the position $\mathbf{r}_i$ of the vertices and cell connectivity.

For this model, the force $\mathbf{F}^i_{\rm vm}$ acting on a particular vertex i can be obtained by taking a derivative of W [13, 15] with respect to the vertex position $\mathbf{r}_i$ as,

$$\mathbf{F}^i_{\rm vm} = -\frac{\partial W}{\partial \mathbf{r}_i} \tag{20a}$$

$$= \eta \frac{d\mathbf{r}_i}{dt}, \tag{20b}$$

and is balanced by the friction force on the vertex from the substrate. Here, η represents effective substrate viscosity experienced by the vertex via cell-substrate friction [15]. A mathematically equivalent description of the vertex model could also be made by using mechanical equilibrium or principle of virtual work [14, 16].

A. Inclusion of active cell stress in the vertex model formulation

Collectively migrating epithelial cells can have an active stress of the form [17]

$$\boldsymbol{\sigma} = \sigma_a(\hat{\mathbf{p}}\hat{\mathbf{p}} - \frac{1}{2}\mathbf{I}), \tag{21}$$

where for $\sigma_a > 0$ and $\sigma_a < 0$, respectively, for contractile and extensile cell active stress. The goal of this section is to present how this stress within a particular cell can be accommodated in the vertex model formalism by obtaining the corresponding active force $\mathbf{F}^i$ on the vertex i of the cell (Figure 7c).

1. *Formulation of obtaining virtual strain of the cell from virtual displacement of cell vertices*

We note that, when the vertices are provided virtual displacement of $\{\delta x^i_\alpha\}$, the total internal virtual work because of the action of the cell active stress $\boldsymbol{\sigma}^\alpha$ on the resulting virtual deformation gradient $\delta\mathbf{u}$ is

$$\delta W_{\rm active} = A\sigma_{\alpha\beta}\delta u_{\alpha\beta} = -\sum_i F^i_\alpha \delta x^i_\beta, \tag{22}$$

where A is the instantaneous area of the cell. We note that the negative sign in front of the summation sign arises since F^i_α is taken as the force exerted by the interior of the cell on the vertices.

If we can find a relation between $\delta u_{\alpha\beta}$ and $\{\delta x^i_\alpha\}$, then Eq. 22 will provide us with expression for F^i_α. We first note that, assuming an affine virtual displacement field, the virtual displacement δx^i_α of any vertex i of a given cell k will be given as

$$\begin{aligned} \delta x^i_\alpha &= \delta u_{\alpha\beta}(x^i_\beta - x^c_\beta) + \delta x^c_\alpha, \text{ and} \\ \delta \rho^i_\alpha &= \delta u_{\alpha\beta}\rho^i_\beta, \end{aligned} \tag{23}$$

where the superscript c denotes the centroid of vertices, with position

$$x^c_\alpha = \frac{1}{N_{\rm ver}} \sum_{i\in{\rm cell}} x^i_\alpha, \tag{24}$$

the virtual displacement of this centroid is

$$\delta x^c_\alpha = \frac{1}{N_{\rm ver}} \sum_{i\in{\rm cell}} \delta x^i_\alpha, \tag{25}$$

and

$$\begin{aligned} \delta \rho^i_\alpha &= \delta x^i_\alpha - \delta x^c_\alpha, \\ \rho^i_\alpha &= x^i_\alpha - x^c_\alpha. \end{aligned} \tag{26}$$

Here, $N_{\rm ver}$ is the number of vertices of the cell under consideration. The connection between $\delta\rho^i_\alpha$ and $\delta u_{\alpha\beta}$ as per Eq. 23 provides a set of $2 \times (N_{\rm ver} - 1)$, independent linear equations, and can be guaranteed a unique solution in

terms of the four independent components of the tensor $\delta u_{\alpha\beta}$, i.e., $\delta u_{11}, \delta u_{12}, \delta u_{21}$ and δu_{22} only for $N_{\text{ver}} = 3$. For $N_{\text{ver}} > 3$, we obtain a solution in the sense of least squares. To do that we minimise the error

$$S = \sum_{i \in \text{cell}} (\delta\rho^i_\alpha - \delta u_{\alpha\beta}\rho^i_\beta)(\delta\rho^i_\alpha - \delta u_{\alpha\gamma}\rho^i_\gamma), \tag{27}$$

where repeated summation is implied over the Greek numerals α, β and γ, which can take values of 1 and 2. This error S is to be minimised over $\delta u_{\mu\nu}$, and will give four independent linear equations. Differentiating S with respect to $\delta u_{\mu\nu}$, we get the following set of equations (in indicial notation)

$$\frac{\partial S}{\partial \delta u_{\mu\nu}} = -2 \sum_{i \in \text{cell}} (\rho^i_\nu \delta\rho^i_\mu - \delta u_{\mu\beta}\rho^i_\beta \rho^i_\nu) = 0. \tag{28}$$

These equations can be written in more readable format in the following manner.

$$\begin{bmatrix} \delta\rho_{11} \\ \delta\rho_{21} \\ \delta\rho_{12} \\ \delta\rho_{22} \end{bmatrix} = \begin{bmatrix} \rho_{11} & \rho_{12} & 0 & 0 \\ \rho_{12} & \rho_{22} & 0 & 0 \\ 0 & 0 & \rho_{11} & \rho_{12} \\ 0 & 0 & \rho_{12} & \rho_{22} \end{bmatrix} \begin{bmatrix} \delta u_{11} \\ \delta u_{12} \\ \delta u_{21} \\ \delta u_{22} \end{bmatrix} \tag{29}$$

where the quantities are defined as follows:

$$\begin{aligned} \rho_\alpha &= \sum_i \rho^i_\alpha = 0, \\ \rho_{\alpha\beta} &= \sum_i \rho^i_\alpha \rho^i_\beta, \\ \delta\rho_{\alpha\beta} &= \sum_i \rho^i_\alpha \delta\rho^i_\beta, \end{aligned} \tag{30}$$

such that $\alpha \in \{1, 2\}$. Equation 29 can be solved to provide the components of δU as follows.

$$\begin{aligned} \delta u_{11} &= \frac{\rho_{12}\delta\rho_{21} - \rho_{22}\delta\rho_{11}}{\rho_{12}^2 - \rho_{11}\rho_{22}}, \\ \delta u_{12} &= \frac{\rho_{12}\delta\rho_{11} - \rho_{11}\delta\rho_{21}}{\rho_{12}^2 - \rho_{11}\rho_{22}}, \\ \delta u_{21} &= \frac{\rho_{12}\delta\rho_{22} - \rho_{22}\delta\rho_{12}}{\rho_{12}^2 - \rho_{11}\rho_{22}}, \\ \delta u_{22} &= \frac{\rho_{12}\delta\rho_{12} - \rho_{11}\delta\rho_{22}}{\rho_{12}^2 - \rho_{11}\rho_{22}}. \end{aligned} \tag{31}$$

Thus in Eq. 31 we have the virtual deformation tensor for a given cell k in terms of the virtual displacement of its vertices $\{\delta\rho^i_\alpha\}$ with respect to its vertex centroid. These expressions are to be substituted in Eq. 22 to find the forces that are exerted on cell vertices due to the active cell stress in Eq. 21.

2. Connection between cell active stress and vertex forces

The active stress for the cell in Eq. 21 can be written in indicial notation as

$$\sigma_{\alpha\beta} = \sigma_a(p_\alpha p_\beta - \frac{1}{2}\delta_{\alpha\beta}), \tag{32}$$

and the contribution to the virtual work is

$$\delta W_{\text{active}} = A\sigma_{\alpha\beta}\delta u_{\alpha\beta}. \tag{33}$$

Using the expression for $\delta u_{\alpha\beta}$ from Eq. 31 we get

$$\begin{aligned} A\sigma_{\alpha\beta}\delta u_{\alpha\beta} &= A\sigma_{11}\delta u_{11} + A\sigma_{12}(\delta u_{12} + \delta u_{21}) + A\sigma_{22}\delta u_{22} \\ &= A\sigma_a(p_1^2 - 1/2)\left(\frac{\rho_{12}\delta\rho_{21} - \rho_{22}\delta\rho_{11}}{\rho_{12}^2 - \rho_{11}\rho_{22}}\right) \\ &+ A\sigma_a(p_2^2 - 1/2)\left(\frac{\rho_{12}\delta\rho_{12} - \rho_{11}\delta\rho_{22}}{\rho_{12}^2 - \rho_{11}\rho_{22}}\right) \\ &+ A\sigma_a(p_1p_2)\left(\frac{\rho_{12}\delta\rho_{11} - \rho_{11}\delta\rho_{21}}{\rho_{12}^2 - \rho_{11}\rho_{22}} + \frac{\rho_{12}\delta\rho_{22} - \rho_{22}\delta\rho_{12}}{\rho_{12}^2 - \rho_{11}\rho_{22}}\right), \\ &= -\sum_{\text{vertices } i} F_\alpha^i \delta x_\alpha^i. \end{aligned} \tag{34}$$

We now note from Eq. 30 that

$$\delta\rho_{\alpha\beta} = \sum_i \rho_\alpha^i(\delta x_\beta^i - \delta x_\beta^c) = \sum_i \rho_\alpha^i \delta x_\beta^i. \tag{35}$$

Using Eq. 35, Eq. 34 is rewritten as

$$\begin{aligned} A\sigma_{\alpha\beta}\delta u_{\alpha\beta} = A\sigma_a \sum_i \Bigg[&\frac{(p_1^2 - 1/2)\left[\rho_{12}\rho_2^i - \rho_{22}\rho_1^i\right] + (p_1p_2)\left[\rho_{12}\rho_1^i - \rho_{11}\rho_2^i\right]}{\rho_{12}^2 - \rho_{11}\rho_{22}}\delta x_1^i \\ &+ \frac{(p_2^2 - 1/2)\left[\rho_{12}\rho_1^i - \rho_{11}\rho_2^i\right] + (p_1p_2)\left[\rho_{12}\rho_2^i - \rho_{22}\rho_1^i\right]}{\rho_{12}^2 - \rho_{11}\rho_{22}}\delta x_2^i \Bigg]. \end{aligned} \tag{36}$$

Hence, from Eqs. 36 and 34 the contribution to the force on vertex i due to the cell active stress from the cell is

$$\begin{aligned} F_1^i &= -A\sigma_a \frac{(p_1^2 - 1/2)\left[\rho_{12}\rho_2^i - \rho_{22}\rho_1^i\right] + (p_1p_2)\left[\rho_{12}\rho_1^i - \rho_{11}\rho_2^i\right]}{\rho_{12}^2 - \rho_{11}\rho_{22}}, \\ F_2^i &= -A\sigma_a \frac{(p_2^2 - 1/2)\left[\rho_{12}\rho_1^i - \rho_{11}\rho_2^i\right] + (p_1p_2)\left[\rho_{12}\rho_2^i - \rho_{22}\rho_1^i\right]}{\rho_{12}^2 - \rho_{11}\rho_{22}}. \end{aligned} \tag{37}$$

It can very easily be seen from Eq. 37 that for a given cell, the sum of all the active forces on the vertices of that cell will be zero. Moreover, the total torque of all these forces with respect to the vertex centroid as defined in Eq. 24 can also be shown to be equal to zero. This is as expected from a symmetric stress tensor. In the current work, we take the cell active stress as extensile, and hence $\sigma_a < 0$ [9].

Finally, the contribution of this active force to any vertex is a vector sum of the force contributions coming from all the cells that the vertex is a part of, and is given by,

$$(F_\alpha^i)^{\text{total}} = \sum_{\text{cell } k \in \text{vertex } i} (F_\alpha^i)^{\text{total}}; \quad \alpha \in \{1, 2\}. \tag{38}$$

The active force on the vertex would be added to the forces from cell area deformation and cell edge contractility as discussed in the earlier section.

B. Polarised or biased edge tensions

It is observed that T1 transitions can be influenced by the polarity of the cells [18]. Such bias in T1 transitions can be introduced in the vertex model by modifying the tension $\lambda_{\alpha\beta}$ of any edge $\alpha\beta$ based on its relative orientation $\hat{\mathbf{e}}_{\alpha\beta}$ with respect to the polarity $\hat{\mathbf{p}}_\alpha$ and $\hat{\mathbf{p}}_\beta$ of the shared cells (Figure 7e) as

$$\Lambda_{\alpha\beta} = \Lambda_{\alpha\beta}^0 + \lambda(1 - [(\hat{\mathbf{e}}_{\alpha\beta} \cdot \hat{\mathbf{p}}_\alpha)^2 + \hat{\mathbf{e}}_{\alpha\beta} \cdot \hat{\mathbf{p}}_\beta)^2]) + \xi(t), \tag{39}$$

where the quantities $\Lambda_{\alpha\beta}^0$, λ, $\xi(t)$ are, respectively, the base edge tension, angle dependent edge tension bias, and correlated noise that is calculated as

$$\frac{d\xi(t)}{dt} = -\frac{1}{\tau}\xi(t) + \gamma(t), \text{ such that} \tag{40}$$

$$\langle\gamma(t)\rangle = 0, \text{ and} \tag{41}$$

$$\langle\gamma(t')\gamma(t'+t)\rangle = \frac{2\Delta\Lambda^2}{\tau}\delta(t). \tag{42}$$

Here, τ and $\Delta\Lambda$ are the correlation time and strength, respectively, for the correlated noise. This noise promotes T1 transitions and introduces tissue fluidity in the vertex model [19]. The angle dependent bias ensure that the edges that are parallel (perpendicular) to the polarisation of the cells have a tension that is lower (higher) by λ than its base value $\Lambda^0_{\alpha\beta}$. This bias enhances the propensity of tissue shear along cell polarisation due to T1 transitions.

C. Inclusion of cell motility

In addition to the forces described in the previous section, cells can also generate motility force [20, 21]. Following the idea of self-propelled cells [22], any cell α can also be modeled to have a speed v_0, such that in the absence of any other forces it moves with a velocity $v_0\hat{\mathbf{p}}_\alpha$, where $\hat{\mathbf{p}}_\alpha$ is the polarisation direction of the cell as described earlier (Figure 7d). A simplest representation of motile force on a particular vertex i is

$$\mathbf{F}^i_{\text{motile}} = \eta v_0 \frac{1}{N_i} \sum_{\text{cell}\,\beta} \hat{\mathbf{p}}_\beta, \tag{43}$$

where N_i is the total number of cells that contain the particular vertex i, and β is the index of each of these cells [23]. The motile force, if included, will be in addition to the forces as described in the previous sections.

D. Dynamical Evolution

Dynamical evolution in these simulations involves updating the position of vertex i as per the following equation

$$\eta \frac{d\mathbf{r}_i}{dt} = \mathbf{F}^i_{\text{basic}} + \mathbf{F}^i_{\text{active}} + \mathbf{F}^i_{\text{motile}}, \tag{44}$$

where the subscripts basic, active, and motile correspond to the contributions to the forces, respectively, from basic vertex model, active stress and biased edge tensions, and cell motility. The evolution of edge tensions is as discussed in the previous section. In addition to the evolution of the vertex positions, whenever the size of any edge becomes smaller than a critical size ϵ_{cls}, a connectivity change, termed as T1 transition in the literature [14, 15], is implemented – the size of the new edge $\epsilon_{\text{opn}} > \epsilon_{\text{cls}}$ (Figure 7f).

The next step is to update the polarisation $\hat{\mathbf{p}}$ of the cells. In our description, the $\hat{\mathbf{p}}^\alpha$ for a given cell α is modeled to have a tendency to align with the orientation of its neighbours (ngb) without distinction between $\hat{\mathbf{p}}^{\text{ngb}}$ and $-\hat{\mathbf{p}}^{\text{ngb}}$. i.e., nematically. This is achieved with the following simple differential equation for $\hat{\mathbf{p}}_\alpha$ of any cell α in the interior:

$$\frac{d\hat{\mathbf{p}}_\alpha}{dt} = (\xi m_{\text{align}} + \xi_{\text{rand}})\hat{\mathbf{p}}^\perp_\alpha, \tag{45}$$

where $\hat{\mathbf{p}}^\perp$ is such that

$$\hat{\mathbf{e}}_z = \hat{\mathbf{p}}_\alpha \times \hat{\mathbf{p}}^\perp_\alpha,$$

the $\hat{\mathbf{e}}_z$ is the vector normal to the plane of the paper.

$$m_{\text{align}} = \hat{\mathbf{e}}_z \cdot \left[\frac{1}{N_\alpha} \sum_{\beta \in \text{ngb}} \text{sign}(\hat{\mathbf{p}}_\alpha \cdot \hat{\mathbf{p}}_\beta)(\hat{\mathbf{p}}_\alpha \times \hat{\mathbf{p}}_\beta) \right]$$

is the rotational torque on $\hat{\mathbf{p}}_\alpha$ and ξ is the alignment rate. The quantity $\text{sign}(\hat{\mathbf{p}}_\alpha \cdot \hat{\mathbf{p}}_\beta)$ ensures that $\hat{\mathbf{p}}_\alpha$ nematically align with polarisation of the N_α neighbours in a mean sense. The orientational noise ξ_{rand} is modeled as uncorrelated Gaussian noise of zero mean and strength D_r. This evolution rule also automatically ensures that the $\hat{\mathbf{p}} \cdot \hat{\mathbf{p}} = 1$ for all the cells. For any cells at the boundary, the only difference is that the alignment torque is

$$m_{\text{align}} = \hat{\mathbf{e}}_z \cdot \text{sign}(\hat{\mathbf{p}}_\alpha \cdot \hat{\mathbf{t}})(\hat{\mathbf{p}}_\alpha \times \hat{\mathbf{t}}),$$

where

$$\hat{\mathbf{t}} = \frac{\mathbf{r}_{\text{next}} - \mathbf{r}_{\text{before}}}{|\mathbf{r}_{\text{next}} - \mathbf{r}_{\text{before}}|},$$

and $\mathbf{r}_{\text{next}}$ and $\mathbf{r}_{\text{before}}$ correspond to the position vectors of the two contiguous cells of cell-α at the boundary.

The initial condition for the positions $\{\mathbf{r}\}$ of the vertices and the polarisation $\{\hat{\mathbf{p}}\}$ of the cells is generated as follows. A confluent colony of 332 cells, a number similar to that observed experimentally, is initially confined within a circular region of radius $R_{\text{colony}} \approx 320$ (see Supplementary Material Section IE for clarification regarding the simulation parameters.) The cells are provided with an initial polarisation $\hat{\mathbf{p}} = \cos\phi_p \hat{\mathbf{e}}_1 + \sin\phi_p \hat{\mathbf{e}}_2$ such that the orientation $\phi_p(x, y)$ is

$$\phi_p(x, y) = \frac{1}{2}\left(\tan^{-1}\left[\frac{y - y_1}{x - x_1}\right] + \tan^{-1}\left[\frac{y - y_2}{x - x_2}\right]\right) + \frac{\pi}{2}, \tag{46}$$

where (x_1, y_1) and (x_2, y_2) is the location of two $+1/2$ defects, which are taken to be symmetrically separated by a distance of $1.6R_{\text{colony}}$ with respect to the center of the circle (also see Supplementary Section ID). An orientation shift of π is randomly added to ϕ_p of individual cells such that the vector sum of $\hat{\mathbf{p}}$ over all the cells is zero. This step is irrelevant for the implementation of forces due to cell active stress and biased edge tensions due to their inherent nematic symmetry (Eqs. 21 and 39) but ensures that the total motile force from all the cells is zero. The cells are then provided with small active stress and evolved under confinement for some time using the above rules till $\{\mathbf{r}\}$ and $\{\mathbf{p}\}$ are almost equilibrated. This configuration is then used as the initial condition for all the numerical experiments, in which the confinement is removed to allow the colonies to elongate (see Movie 7). Different simulation conditions correspond to varying proportion of active cell stress, biased cell edge tension and cell motility. The results from the simulations are then analysed in a similar manner as for the experimental data (Figure 7 – figure supplement 1).

This set of polarity evolution rules for the interior and the boundary cells ensure that in the steady-state the orientation field ϕ_p satisfies in a coarse-grained sense, i.e., on longer length-scales, the Laplace equation $\nabla^2\phi_p = 0$. The nematic field for the interior cells tends to have a uniform orientation, whereas the nematic field for the boundary cells tries to align along the colony boundary. Because of this boundary alignment tendency of the border cells, at least for the parameters used in our simulations (Supplementary Material Section IE), the total topological charge of the polarisation field is mostly conserved in our simulations, i.e., remains equal to the total initial charge of $+1$ (for a relevant study in another context see Ref. [24].) Due to the action of active cell stress (Eq. 21) the cells have a tendency to elongate predominantly along $\hat{\mathbf{p}}$ thus creating a cell-shape nematic orientation field $\mathbf{q} = \cos\phi\hat{\mathbf{e}}_1 + \sin\phi\hat{\mathbf{e}}_2$ (also see Supplementary Material Sections IA-C.) Hence, the cell elongation anisotropy, as described earlier in Supplementary Material Sections IC and ID, can loosely be thought of to be a readout of the internal polarisation of the cells. However, since the actual cell shape results from the interplay between cell mechanical properties and active cell stress, $\hat{\mathbf{p}}$ and $\mathbf{q}$ are not necessarily always fully aligned. Thus, for the cell-shape nematic field, the total topological charge can be less than $+1$ if the aligning tendency of internal cells dominates, e.g., when the cell active stress is large (see Movie 7).

E. Parameters used and the non-dimensional groups present in the Vertex Model

Using reference scales for length (l_0), time (t_0) and energy (U_0), we get the following set of non-dimensional groups for the various parameters that are involved in the simulations. The non-dimensional counterparts of the parameters used in the simulations have been assigned an additional $'$ to make them distinct from the original.

1. Substrate friction: $\frac{\eta l_0^2}{t_0 U_0} \to \eta' = 1000$
2. Area modulus: $\frac{K l_0^4}{U_0} \to K' = 0.1$
3. Cell preferred area: $\frac{A_0}{l_0^2} \to A_0' = 1000$
4. Edge contractility: $\frac{\Lambda_0 l_0}{U_0} \to \Lambda_0' = 100$, $\frac{\Delta\Lambda l_0}{U_0} \to \Delta\Lambda = 20$, $\frac{\lambda l_0}{U_0} \to \lambda' \in [0, 45]$
5. Cellular active stress (negative sign indicates extensile): $\frac{\sigma_a l_0^2}{U_0} \to \sigma_a' \in [-8, 0]$.
6. Motility: $\frac{v_0 t_0}{l_0} \to v_0' = 0.05$
7. Polarisation alignment rate: $\xi t_0 \to \xi' = 0.03$
8. Strength of Gaussian noise for polarisation: $t_0 D_r \to D_r' = 2.7 \times 10^{-6}$ (very small)
9. Relaxation time for edge tension fluctuations: $\frac{\tau}{t_0} \to \tau' = 10^3$

10. Total experimental time: $\frac{T_{\text{total}}}{t_0} \to T'_{\text{total}} = 4000$
11. T1 transition cutoffs: $\frac{\epsilon_{\text{opn}}}{l_0} \to \epsilon'_{\text{opn}} = 6$ and $\frac{\epsilon_{\text{cls}}}{l_0} \to \epsilon'_{\text{cls}} = 4$
12. Colony size: $\frac{R_{\text{colony}}}{l_0} \to R'_{\text{colony}} = 317$
13. Simulation time-step: $\frac{\Delta t}{t_0} \to \Delta t' = 1$

We can now choose the scales l_0, t_0, and U_0. We use the simulation time-step $\Delta t' = 1$. We get the values of total cumulative shear in the range $\approx 0.05 - 0.2$ that is comparable with the experimental values at the end of the 4000 simulation time. Since the total duration of the experiment is 2 hrs, this implies that $t_0 \approx 1.8$ s in experimental units. We also know from the experiments that the area of one cell is $\approx 400\ \mu\text{m}^2$. Since, within our simulations, the preferred area of cells is taken as $A_0 = 1000$, this implies that $l_0 \approx 0.63\ \mu$m.

The energy (or force) scale can be chosen arbitrarily since it is present in both the left hand and the right hand sides of Eq. 44, and must only be chosen consistently. We now figure out the relative contributions to the forces that can come from different components for a cell: motile force, active force, basic edge contractility, active edge contractility, and isotropic force. For the values used the non-dimensional (simulation) values are:

1. cell motile force: $\approx \eta' v'_0 = 1000 \times [0, 0.05] = [0, 50]$
2. cell active force (extensile): $\approx |\sigma'_a \sqrt{A'_0}| = [0, 8] \times \sqrt{1000} \approx [0, 250]$
3. basic edge tension: $\Lambda'_0 = 100$
4. biased edge tension: $\approx \lambda' = [0, 45]$
5. cell area stress: $K' \sqrt{A'_0} \Delta A' \approx 3.16 \times [0, 15] \approx [0, 45]$

One can see that forces from all these sources are of the same order of magnitude. Specifically when we wish to compare the relative magnitudes of active edge contractility and the active stress, a quantity of relevance is $\frac{\lambda'}{\sigma'_a \sqrt{A'_0}}$. The values of the active terms σ'_a, λ' and v'_0 used in the simulations are shown in Figure 7 – figure supplement 1.

---

[1] B. Aigouy, R. Farhadifar, D. B. Staple, A. Sagner, J.-C. Röper, F. Jülicher, and S. Eaton, Cell **142**, 773 (2010).
[2] B. Aigouy, D. Umetsu, and S. Eaton, in *Drosophila* (Springer, 2016), pp. 227–239.
[3] M. Merkel, R. Etournay, M. Popović, G. Salbreux, S. Eaton, and F. Jülicher, Physical Review E **95**, 032401 (2017).
[4] R. Etournay, M. Merkel, M. Popović, H. Brandl, N. A. Dye, B. Aigouy, G. Salbreux, S. Eaton, and F. Jülicher, eLife **5**, e14334 (2016).
[5] E. Paluch and C.-P. Heisenberg, Curr. Biol. **19**, R790 (2009).
[6] M. Rauzi and P.-F. Lenne, Curr Top Dev Biol **95**, 93 (2011).
[7] R. Etournay, M. Popović, M. Merkel, A. Nandi, C. Blasse, B. Aigouy, H. Brandl, G. Myers, G. Salbreux, F. Jülicher, et al., eLife **4**, e07090 (2015).
[8] Z. Püspöki, M. Storath, D. Sage, and M. Unser, in *Focus on Bio-Image Informatics* (Springer, 2016), pp. 69–93.
[9] T. B. Saw, A. Doostmohammadi, V. Nier, L. Kocgozlu, S. Thampi, Y. Toyama, P. Marcq, C. T. Lim, J. M. Yeomans, and B. Ladoux, Nature **544**, 212 (2017).
[10] MATLAB, *version 9.4.0 (R2018a)* (The MathWorks Inc., Natick, Massachusetts, 2018).
[11] M. Kleman and O. D. Laverntovich, *Soft matter physics: an introduction* (Springer Science & Business Media, 2003).
[12] P.-G. De Gennes and J. Prost, *The physics of liquid crystals*, vol. 83 (Oxford university press, 1995).
[13] R. Farhadifar, J.-C. Röper, B. Aigouy, S. Eaton, and F. Jülicher, Curr. Biol. **17**, 2095 (2007).
[14] S. Alt, P. Ganguly, and G. Salbreux, Philosophical Transactions of the Royal Society B: Biological Sciences **372**, 20150520 (2017).
[15] A. G. Fletcher, M. Osterfield, R. E. Baker, and S. Y. Shvartsman, Biophys. J. **106**, 2291 (2014).
[16] H. H. Chen and G. W. Brodland, Journal of biomechanical engineering **122**, 394 (2000).
[17] M. Popović, A. Nandi, M. Merkel, R. Etournay, S. Eaton, F. Jülicher, and G. Salbreux, New Journal of Physics **19**, 033006 (2017).
[18] K. Sato, T. Hiraiwa, E. Maekawa, A. Isomura, T. Shibata, and E. Kuranaga, Nature communications **6**, 10074 (2015).
[19] S. Curran, C. Strandkvist, J. Bathmann, M. de Gennes, A. Kabla, G. Salbreux, and B. Baum, bioRxiv p. 078204 (2016).
[20] A. Mogilner and G. Oster, Biophys. J. **71**, 3030 (1996).
[21] T. D. Pollard and G. G. Borisy, Cell **112**, 453 (2003).
[22] D. Bi, X. Yang, M. C. Marchetti, and M. L. Manning, Physical Review X **6**, 021011 (2016).
[23] D. M. Sussman, Computer Physics Communications **219**, 400 (2017).
[24] R. M. W. van Bijnen, R. H. J. Otten, and P. van der Schoot, Phys. Rev. E **86**, 051703 (2012).